machines

MDPI

Article

Adaptive Sampling-Time Multivector Model Predictive Control for Six-Phase Induction Motor Drives

Rafael Lara-Lopez [1], Ignacio Gonzalez-Prieto [1,*], Juan Carrillo-Rios [1,*], Juan Jose Aciego [1], Pablo Mora-Moreno [1], Mario J. Duran [1] and Angel Gonzalez-Prieto [2]

[1] Department of Electrical Engineering, University of Malaga, 29071 Malaga, Spain; rafalalopez27@uma.es (R.L.-L.); juanjoseaciego@uma.es (J.J.A.); pmoram.w@uma.es (P.M.-M.); mjduran@uma.es (M.J.D.)
[2] Department of Electrical Engineering, Polytechnic University of Madrid, 28040 Madrid, Spain; angel.gprieto@upm.es
* Correspondence: igp@uma.es (I.G.-P.); juan.carrillo.rios@uma.es (J.C.-R.)

Abstract

Multiphase electric drives have gained significant attention in recent years due to their enhanced efficiency and inherent fault-tolerant capability, making them a promising solution for modern high-performance applications. In this context, finite control set model predictive control (FCS-MPC) has emerged as an effective control strategy due to its flexibility in handling multivariable systems and multiple control objectives. Among its recent developments, variable-sampling-time approaches introduce an additional degree of freedom that enables more efficient adaptation of the control action, particularly reducing switching frequency. This variant of FCS-MPC schemes is based on a sequential structure, in which the direction of the desired current response is prioritized over its magnitude, even when implementation constraints limit its achievement. This work proposes an adaptive sampling time multivector model predictive control strategy (AST-MPC) for six-phase induction motor (6ph-IM) drives. The proposed AST-MPC combines multivector control actions with a threshold-based mechanism to incorporate magnitude information into the selection of control actions, typically governed by directional criteria. The designed approach is experimentally validated and compared under steady-state and transient conditions using multiple performance metrics. Results demonstrate that AST-MPC achieves improved current quality and reduced switching frequency, maintaining suitable dynamic performance and providing natural fault tolerance.

Keywords: model predictive control schemes; multiphase electric drives; multivector solutions; variable sampling time strategies

Check for updates

Academic Editor: Mohamed Abdelrahem

Received: 13 April 2026
Revised: 21 May 2026
Accepted: 22 May 2026
Published: 26 May 2026

Copyright: © 2026 by the authors. Licensee MDPI, Basel, Switzerland. This article is an open access article distributed under the terms and conditions of the Creative Commons Attribution (CC BY) license.

1. Introduction

In recent decades, multiphase electric drives (EDs) have evolved from primarily academic concepts into a viable industrial alternative to their three-phase counterparts [1–5]. Several advantages, such as higher power density, lower per-phase power ratings, reduced torque ripple, alleviated semiconductor voltage and current stress for the same power level [6], and enhanced fault tolerance [7] make them ideal for a wide range of industrial applications. Certain sectors, such as automotive [1,2,8,9] and wind energy systems [10], have adopted this technology in high-profile products. Both ED technologies are typically implemented using voltage source converters (VSCs). Typically, when the number of phases is a multiple of three, they are developed by associating three-phase VSCs to

match the required number of system phases [9,11]. The requirement of multiphase EDs increases the complexity of control schemes due to the appearance of additional degrees of freedom [6,11]. Conventionally, multiphase EDs have been controlled using strategies with explicit modulation stages [6,12–14]. Nonetheless, in recent years, direct control approaches, particularly finite control set model predictive control (FCS-MPC), have attracted significant interest [15–20]. These have proven highly effective due to their ability to deal with multiple variables and optimize multiple objectives in a straightforward manner [21]. They also offer improved current dynamic performance due to better DC-link utilization, without requiring overmodulation strategies. However, despite the aforementioned advantages, conventional FCS-MPC algorithms, which apply a single vector per control period, exhibit several limitations.

On the one hand, the application of a single control action leads to a conflict between control objectives. It is well known that the available voltage vectors in a multiphase VSC can be simultaneously projected onto different orthogonal subspaces with physical significance [6,22,23]. For instance, in several multiphase motors with distributed-winding stators, the application of a voltage vector results in simultaneous projections onto multiple subspaces [24]. The projection onto the $\alpha\beta$ subspace is responsible for torque and flux production. In contrast, voltage components that appear in the secondary subspaces are not involved in electromechanical energy conversion and are associated exclusively with copper losses [6]. Therefore, both control objectives become incompatible when addressed simultaneously, leading to unacceptable phase current quality and inadequate reference tracking, particularly in multiphase ED with low-impedance secondary planes. Thus, the control scheme may further increase the VSC switching frequency as a consequence of correcting errors arising from conflicting regulation objectives [25]. In this context, the impact of this control objective conflict is inherently amplified by the fixed sampling time used to apply the control action in standard FCS-MPC, increasing the harmonic injection in secondary subspaces [26]. On the other hand, beyond the inherent conflict between control objectives arising from applying a single control action per sampling period, the use of the full set of available voltage vectors in the VSC also poses a significant challenge for standard FCS-MPC [27]. In this case, all possible voltage vectors must be evaluated during the optimization process, resulting in a high computational burden [28]. This issue becomes particularly critical in multiphase systems, where the number of candidate control actions increases exponentially with the number of phases [27,29].

Considerable work has been carried out to address the aforementioned limitation related to FCS-MPC. Multivector solutions have proven effective in overcoming certain drawbacks of standard FCS-MPC [22,27,30–32]. These approaches apply more than one control action within a single control period. Such actions are suitably synthesized to cancel, or at least minimize, the average voltage production in the secondary subspace while maximizing torque and flux generation, thereby resulting in an open-loop control of the secondary components. For instance, in asymmetrical six-phase drives, both large and medium-large voltage vectors have been considered. However, the significant voltage contribution of the latter in the xy subspace leads to a high injection of harmonic currents, resulting in the so-called average deception [20,27,31–37]. Consequently, regardless of the number of phases, large voltage vectors are typically preferred due to their favorable voltage ratio $R_{\alpha\beta}$ [22] between the main and secondary subspaces [7,30,36,38], thus minimizing copper losses in distributed-winding machines. The use of control actions composed of large voltage vectors not only ensures high flux/torque production while limiting the voltage output in the secondary plane, but also provides two additional benefits. Firstly, it extends the speed range by maximizing dc-link voltage utilization. Secondly, it reduces the switching frequency, since there is one switch transition when the next vector is an adjacent

large vector. In this context, works such as [7,39–41] have effectively improved phase current quality while providing an inherent natural fault-tolerant capability. In contrast, other approaches, e.g., [42], also adopt multivector control actions but regulate the secondary subspace currents in a closed-loop manner in order to mitigate VSC nonlinearities, thus sacrificing this natural fault tolerance.

Other studies have addressed the limitations of standard FCS-MPC in multiphase EDs by extending the prediction horizon. In the prediction stage, the conventional approach estimates currents up to $k+2$. Extending the prediction horizon to $k+3$ has been shown to improve performance in both classical FCS-MPC and multivector schemes, particularly at low operating speeds [43]. However, the associated computational burden limits the feasibility of achieving further performance gains using these solutions.

Another approach aimed at overcoming the limitations of standard FCS-MPC focuses on a different key parameter in the prediction-stage expressions: the sampling time. This method decouples the selection of the control action from the application time, and they are commonly termed variable sampling time lead pursuit control (VSTLPC). Initially introduced by [44] and further developed in VSTLPC [45] or [25], it computes the application time using a non-iterative method based on the system derivative and implemented using a rotor current observer. The same authors in [26] introduce a new stage in the VSTLPC scheme to refine the computation of the variable sampling time presented in [45]. In this work, improvements over the FCS-MPC control scheme are achieved by incorporating this additional degree of freedom provided by the variable sampling time. In [46], the objective is to reduce the high computational burden associated with conventional FCS-MPC by employing a region-based selection approach. This selection is addressed using a deadbeat strategy and a rotor variable observer. Ref. [47] presents a combined approach to overcome the limitations of FCS-MPC by leveraging both the multivector strategy and the flexibility of variable sampling time. In particular, the control actions included in [47] are formed by combining voltage vectors aligned in the principal plane with different magnitudes in a five-phase electric drive, and the results are validated through simulations. This approach inevitably leads to a high level of harmonic distortion due to average deception [22]. The effect becomes more pronounced in the low-impedance xy subspace. Regardless of the considered VSTLP schemes, all of them are based on a sequential algorithm in which the selected control action is chosen only by considering the required direction, whereas the desired magnitude is satisfied only with the estimation of the sampling period [25,26,44–47]. This approach can lead to a suboptimal selection process, as the voltage magnitude is neglected in the estimation of the optimal control action. Consequently, the switching activity is generally increased, which, far from improving the current quality, may actually deteriorate it because the control scheme must compensate for previously applied unsuitable voltage vectors. In addition, in multiphase drives, a double control conflict can arise when the required control action and the applied sampling time differ across subspaces. For instance, the regulation of secondary subspaces commonly requires shorter application times, whereas flux and torque production demand longer control periods.

Under this framework, this paper proposes an adaptive sampling-time model predictive control strategy, referred to as AST-MPC, to overcome the aforementioned limitations of conventional FCS-MPC and VST-based approaches (see Table 1). The proposed method combines adaptive sampling time with a structured multivector control framework and an enhanced decision mechanism to improve control performance in multiphase electric drives. The effectiveness and feasibility of the proposed strategy have been experimentally validated on a six-phase electric drive test bench.

The main contributions of this work can be summarized as follows:

- The designed AST-MPC enables, for the first time (see Table 1), the joint consideration of directional alignment and current magnitude during the control action selection process, thereby overcoming the limitations of purely direction-based criteria.
- The integration of predefined virtual voltage vectors within a variable sampling time framework, enabling open-loop regulation of the secondary subspace while reducing the number of controller conflicts and candidate control actions. This feature preserves the inherent fault-tolerant capability of multiphase drives without requiring control reconfiguration.
- The experimental validation of the proposed AST-MPC in a six-phase electric drive, demonstrating its effectiveness in mitigating control conflicts between subspaces and improving current quality compared to existing VST-MPC and multivector approaches.

The remainder of the paper is organized as follows. Section 2 summarizes the fundamentals of six-phase induction motor drive systems. Section 3 reviews variable-sampling-time approaches for multiphase electric drives. Experimental results and conclusions are presented in Section 4 and Section 5, respectively.

Table 1. Comparative analysis of VSTLP-MPC solutions for multiphase drives.

Ref.	*n*-Phase	VST	Non-Sequential Mechanism	Virtual Vectors †	Natural Fault Tolerance †
[25]	5	✓	✗	✗	✗
[26]	5	✓	✗	✗	✗
[44]	3	✓	✗	✗	✗
[45]	5	✓	✗	✗	✗
[46]	5	✓	✗	✗	✗
[47]	5	✓	✗	✗	✗
Proposed	6	✓	✓	✓	✓

† Experimentally validated.

2. Six-Phase Induction Motor Drive

2.1. Topology Description

The studied drive consists of an asymmetrical six-phase induction machine (IM) supplied by a dual three-phase two-level voltage source converter (VSC), as shown in Figure 1. The stator is formed by two three-phase windings spatially shifted by 30° and configured with isolated neutral points. This prevents current circulation between both windings.

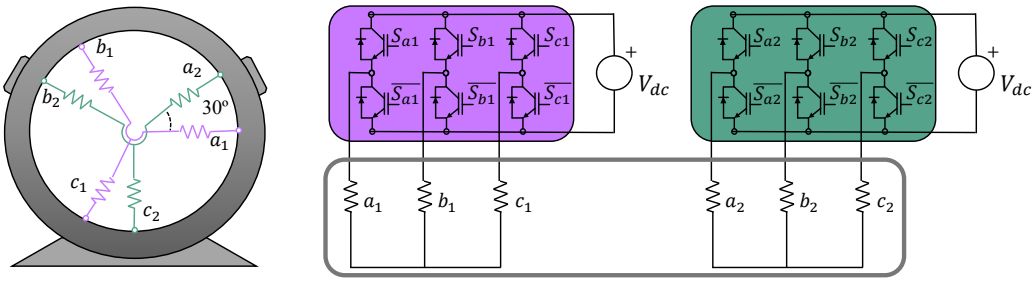


Figure 1. Schematic diagram of the six-phase IM drive topology.

The power stage consists of two conventional three-phase two-level VSCs, each supplied by an independent dc-link at the same voltage level V_{dc}. The dual VSC provides $2^6 = 64$ possible switching states. The switching configuration is described by a binary vector $[S]$, whose elements S_{ij} define each VSC phase state. Subscript $i \in a, b, c$ denotes the phase, while $j \in 1, 2$ identifies the stator winding. When $S_{ij} = 1$, the upper semiconductor

of the VSC leg is conducting, and the lower one is turned off. Conversely, $S_{ij} = 0$ indicates the complementary state.

Under this notation, the stator phase voltages (v_{ij}) can be expressed as a function of the switching vector $[S]$ and the DC-link voltage V_{dc}:

$$\begin{bmatrix} v_{a1} \\ v_{b1} \\ v_{c1} \\ v_{a2} \\ v_{b2} \\ v_{c2} \end{bmatrix} = \frac{V_{dc}}{3} \begin{bmatrix} 2 & -1 & -1 & 0 & 0 & 0 \\ -1 & 2 & -1 & 0 & 0 & 0 \\ -1 & -1 & 2 & 0 & 0 & 0 \\ 0 & 0 & 0 & 2 & -1 & -1 \\ 0 & 0 & 0 & -1 & 2 & -1 \\ 0 & 0 & 0 & -1 & -1 & 2 \end{bmatrix} \begin{bmatrix} S_{a1} \\ S_{b1} \\ S_{c1} \\ S_{a2} \\ S_{b2} \\ S_{c2} \end{bmatrix} \tag{1}$$

Although the phase-domain model fully characterizes the drive, alternative reference frames simplify the analysis and control design. In multiphase EDs, vector space decomposition (VSD) projects phase variables onto three orthogonal subspaces with clear physical meaning [24].

By applying the amplitude-invariant Clarke transformation (2), phase voltages are expressed in VSD variables (3), yielding three orthogonal subspaces. The primary $\alpha\beta$ plane contains flux- and torque-producing components, whereas the secondary xy subspace is associated with stator copper losses in distributed-winding machines. The transformation also yields zero-sequence components. Due to isolated neutrals, zero-sequence currents do not circulate through the stator windings.

$$[\mathbf{C}] = \frac{1}{3} \begin{bmatrix} 1 & -1/2 & -1/2 & \sqrt{3}/2 & -\sqrt{3}/2 & 0 \\ 0 & \sqrt{3}/2 & -\sqrt{3}/2 & 1/2 & 1/2 & -1 \\ 1 & -1/2 & -1/2 & -\sqrt{3}/2 & \sqrt{3}/2 & 0 \\ 0 & -\sqrt{3}/2 & \sqrt{3}/2 & 1/2 & 1/2 & -1 \\ 1 & 1 & 1 & 0 & 0 & 0 \\ 0 & 0 & 0 & 1 & 1 & 1 \end{bmatrix}, \tag{2}$$

$$\left[v_\alpha, v_\beta, v_x, v_y, v_{z1}, v_{z2}\right]^{\mathrm{T}} = [\mathbf{C}] \cdot \left[v_{a1}, v_{b1}, v_{c1}, v_{a2}, v_{b2}, v_{c2}\right]^{\mathrm{T}}. \tag{3}$$

After applying the Clarke transformation, each available switching state can be mapped to a voltage vector in both the $\alpha\beta$ and xy subspaces. The distribution of these vectors is depicted in Figure 2. Based on their magnitude in the main plane, vectors are classified into five groups: large (V_L), medium-large (V_{ML}), medium (V_M), small (V_S), and null vectors (V_0).

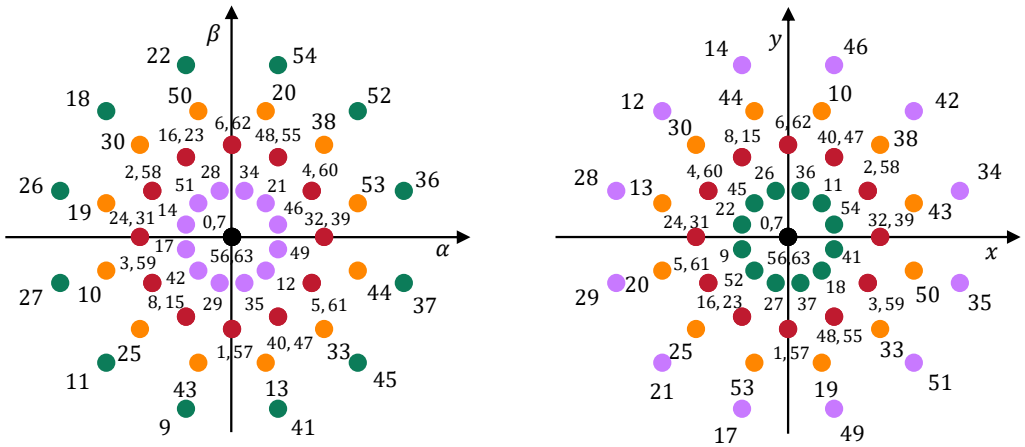


Figure 2. Voltage vectors maps ($\alpha\beta$ and xy) generated by the admissible switching configurations of a dual three-phase two-level VSC after applying VSD to supply an asymmetrical 6ph-IM.

As shown in Figure 2, large vectors provide the highest $\alpha\beta$ amplitude while maintaining relatively low xy components. This property leads to improved dc-link voltage utilization and reduced harmonic-related copper losses. For this reason, this subset of switching states is typically selected when active control action is required [48]. The set of selectable control actions is typically complemented by the null voltage vector, as this switching state yields zero contribution in both subspaces [30].

For control purposes, further decoupling of electromagnetic variables is achieved by projecting the stationary $\alpha\beta$ components onto a synchronously rotating reference frame using the Park transformation matrix defined in (4). The angle θ_s defines the position of the reference frame and can be calculated from the measured speed and estimated slip [49]. The resulting relationship, given in (5), expresses voltages or currents (i) in the rotating dq frame:

$$[D] = \begin{bmatrix} \cos\theta_s & \sin\theta_s \\ -\sin\theta_s & \cos\theta_s \end{bmatrix}, \tag{4}$$

$$\begin{bmatrix} i_d, i_q \end{bmatrix}^T = [D] \cdot \begin{bmatrix} i_\alpha, i_\beta \end{bmatrix}^T. \tag{5}$$

In this synchronous frame, the d-axis component is directly associated with flux production, whereas the q-axis component governs electromagnetic torque generation. This decoupling simplifies control implementation and serves as the basis for the proposed predictive strategy.

2.2. Machine Model

The IM model can be represented by the equivalent circuits shown in Figure 3, based on the stationary $\alpha\beta$ reference frame after applying the Clarke transformation. For control implementation purposes, the motor equations are typically discretized and expressed in state-space form [50]:

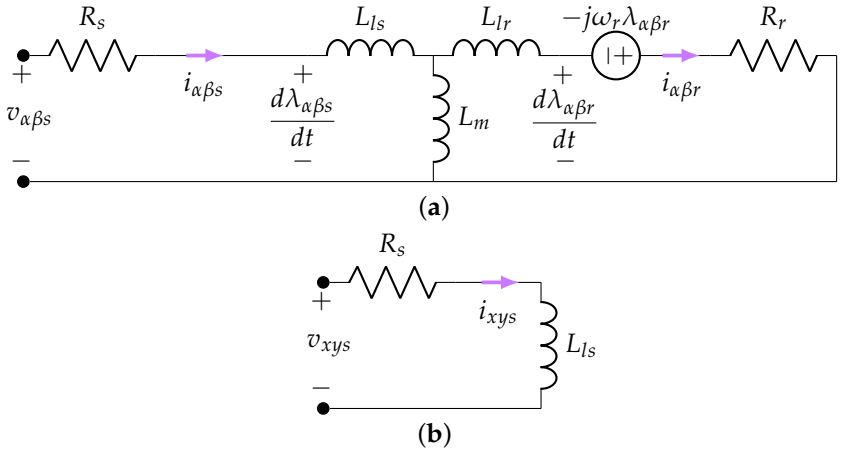


Figure 3. Equivalent circuit in a stationary reference frame of a six-phase IM with squirrel-cage rotor: (**a**) $\alpha\beta$ subspace and (**b**) xy subspace.

$$\begin{aligned} \frac{d}{dt}\Big[X\Big] &= \Big[A\Big] \cdot \Big[X\Big] + \Big[B\Big] \cdot \Big[U\Big], \\ \Big[U\Big] &= \Big[v_{\alpha s}, v_{\beta s}, v_{xs}, v_{ys}, 0, 0\Big]^T, \\ \Big[X\Big] &= \Big[i_{\alpha s}, i_{\beta s}, i_{xs}, i_{ys}, \lambda_{\alpha r}, \lambda_{\beta r}\Big]^T, \end{aligned} \tag{6}$$

where λ is the magnetic flux. The subscripts $\alpha\beta$ and xy identify the corresponding subspaces, while the subscripts s and r denote stator- and rotor-related variables, respectively.

The matrices $[A]$ and $[B]$ describe the dynamic behavior of the multiphase motor, and their coefficients are directly related to the machine parameters:

$$[A] = \begin{bmatrix} a_0 & 0 & 0 & 0 & b_0 & f_0 \cdot \omega_r \\ 0 & a_0 & 0 & 0 & -f_0 \cdot \omega_r & b_0 \\ 0 & 0 & c_0 & 0 & 0 & 0 \\ 0 & 0 & 0 & c_0 & 0 & 0 \\ d_0 & 0 & 0 & 0 & e_0 & -\omega_r \\ 0 & d_0 & 0 & 0 & \omega_r & e_0 \end{bmatrix}, [B] = \begin{bmatrix} g_0 & 0 & 0 & 0 \\ 0 & g_0 & 0 & 0 \\ 0 & 0 & h_0 & 0 \\ 0 & 0 & 0 & h_0 \\ 0 & 0 & 0 & 0 \\ 0 & 0 & 0 & 0 \end{bmatrix}, \tag{7}$$

$$\begin{array}{llll} \sigma = 1 - \dfrac{L_m^2}{L_r \cdot L_s} & \tau_r = \dfrac{L_r}{R_r} & \tau_s = \dfrac{L_s}{R_s} & \tau_{ls} = \dfrac{L_{ls}}{R_s} \\ a_0 = -\left(\dfrac{1}{\sigma \cdot \tau_s} + \dfrac{1-\sigma}{\sigma \cdot \tau_r}\right) & b_0 = \dfrac{1-\sigma}{\tau_r \cdot \sigma \cdot L_m} & c_0 = -\dfrac{1}{\tau_{ls}} & d_0 = \dfrac{L_m}{\tau_r} \\ e_0 = -\dfrac{1}{\tau_r} & f_0 = \dfrac{1-\sigma}{\sigma \cdot L_m} & g_0 = \dfrac{1}{\sigma \cdot L_s} & h_0 = \dfrac{1}{L_{ls}} \end{array} \tag{8}$$

where ω_r is the electrical rotor speed; R is the resistance; L_l is the leakage inductance; and L_m is the mutual inductance.

Once the machine model has been expressed in state variables, it needs to be discretized to enable its implementation in real-time digital control systems. Several discretization techniques are discussed in the literature, such as the Crank-Nicolson method, the Adams-Bashforth method, or the Forward Euler method [51]. Due to its simplicity and its satisfactory performance in first-order systems, the Forward Euler method has been selected for this work [52]. This method approximates the derivative as the ratio between increment and time step, as expressed in (9):

$$\begin{aligned} \frac{d}{dt}\Big[X\Big] &\approx \frac{\Delta X(t)}{\Delta t}, \\ \Delta X(t) &= X(t + \Delta t) - X(t). \end{aligned} \tag{9}$$

This expression is valid for sufficiently small time increments. In the case of FCS-MPC-based control strategies, this time increment (Δt) corresponds to the sampling period at which the control algorithm is executed, denoted as T_s. By applying the derivative approximation (9) to the continuous-time state-space (6), Equation (10) can be obtained:

$$\frac{\Big[X(t + \Delta t) - X(t)\Big]}{T_s} = \Big[A\Big] \cdot \Big[X(t)\Big] + \Big[B\Big] \cdot \Big[U(t)\Big] \tag{10}$$

Defining k as the current time instant and $k+1$ as the future instant after a time interval T_s, Equation (10) can be rewritten as

$$\begin{aligned} \frac{\Big[X(k+1) - X(k)\Big]}{T_s} &= \Big[A\Big] \cdot \Big[X(k)\Big] + \Big[B\Big] \cdot \Big[U(k)\Big], \\ \Big[X(k+1) - X(k)\Big] &= T_s \cdot \Big[A\Big] \cdot \Big[X(k)\Big] + T_s \cdot \Big[B\Big] \cdot \Big[U(k)\Big], \\ \Big[X(k+1)\Big] &= \Big(\Big[I\Big] + T_s \cdot \Big[A\Big]\Big) \cdot \Big[X(k)\Big] + T_s \cdot \Big[B\Big] \cdot \Big[U(k)\Big]. \end{aligned} \tag{11}$$

This formulation leads to a discrete-time model of the machine, which allows the computation of future current states based on the present current values, the applied voltage vector, and the electrical rotor speed. The resulting predictive model constitutes the keystone of FCS-MPC-based strategies. For the sake of clarity, the matrix expression presented above is further expanded:

$$
\begin{aligned}
i_\alpha(k+1) &= (1+T_s\cdot a_0)\cdot i_\alpha(k) + T_s\cdot\big(b_0\cdot\lambda_\alpha(k) + f_0\cdot\omega_r\cdot\lambda_\beta(k)\big) + T_s\cdot g_0\cdot v_\alpha(k),\\
i_\beta(k+1) &= (1+T_s\cdot a_0)\cdot i_\beta(k) + T_s\cdot\big(-f_0\cdot\omega_r\cdot\lambda_\alpha(k) + b_0\cdot\lambda_\beta(k)\big) + T_s\cdot g_0\cdot v_\beta(k),\\
i_x(k+1) &= (1+T_s\cdot c_0)\cdot i_x(k) + T_s\cdot h_0\cdot v_x(k),\\
i_y(k+1) &= (1+T_s\cdot c_0)\cdot i_y(k) + T_s\cdot h_0\cdot v_y(k),\\
\lambda_\alpha(k+1) &= (1+T_s\cdot e_0)\cdot\lambda_\alpha(k) + T_s\cdot\big(d_0\cdot i_\alpha(k) - \omega_r\cdot\lambda_\beta(k)\big),\\
\lambda_\beta(k+1) &= (1+T_s\cdot e_0)\cdot\lambda_\beta(k) + T_s\cdot\big(d_0\cdot i_\beta(k) + \omega_r\cdot\lambda_\alpha(k)\big).
\end{aligned}
\tag{12}
$$

where the predictive model is written explicitly on a per-equation basis for each state variable.

3. Variable Sampling Time Control Schemes in Multiphase Drives

3.1. Theoretical Principles

FCS-MPC-based schemes traditionally operate with a fixed sampling period, meaning that switching decisions are evaluated at uniformly spaced time instants. In contrast, variable sampling time predictive control strategies introduce the sampling interval as an additional degree of freedom in the control law. Instead of assuming a fixed control period, the regulation algorithm determines both the optimal switching state and the period during which it should be applied. This time interval is restricted to a predefined admissible range defined by a minimum and a maximum sampling period, T_{min} and T_{max}, respectively. This approach enables the regulation scheme to adapt the control frequency to the instantaneous operating conditions of the drive while preserving the predictive control framework.

The structure of variable-sampling-time control schemes typically involves two well-defined selection processes [26]: one dedicated to determining the control action and another responsible for selecting the control period, i.e., the time during which the selected action will be applied. Prior to these two decision stages, the desired reference current vector is estimated to define the ideal direction of the stator currents in the next control step. This vector can be obtained as the difference between the reference currents at the next control instant and the measured current values, as illustrated in Figure 4 by the green line. As multiple orthonormal subspaces appear, a reference current vector can be estimated for each plane as follows:

$$
\begin{aligned}
\Delta i_{\alpha\beta} &= i^*_{\alpha\beta}(k+1) - i_{\alpha\beta}(k),\\
\Delta i_{xy} &= i^*_{xy}(k+1) - i_{xy}(k)
\end{aligned}
\tag{13}
$$

where $i^*_{\alpha\beta}(k+1)$ and $i^*_{xy}(k+1)$ represent the reference current vectors for the next control instant, whereas $i_{\alpha\beta}(k)$ and $i_{xy}(k)$ denote the measured stator current vector at the current sampling instant.

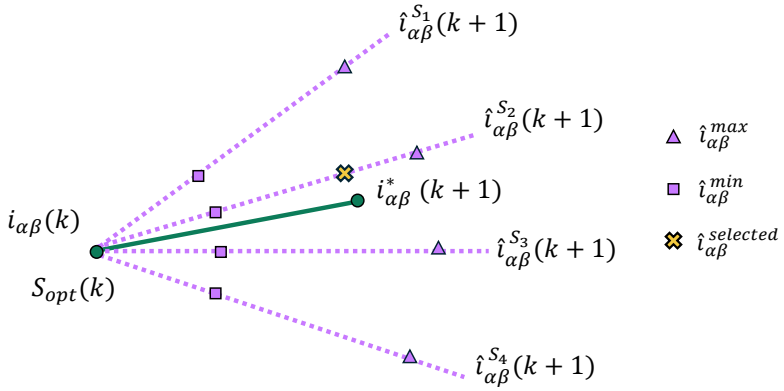


Figure 4. Control law of variable sampling time control schemes.

Once the reference current vectors $\Delta i_{\alpha\beta}$ and Δi_{xy} have been obtained, the first selection stage begins, which is responsible for determining the control action to be applied. The criterion in [26], forming the basis for the proposal developed in this work, consists of selecting the voltage vector whose predicted current response exhibits the closest alignment with the reference current direction. For that purpose, the n available control actions are employed to estimate the predicted current response in the different subspaces, $\hat{\imath}^{n}_{\alpha\beta}(k)$ and $\hat{\imath}^{n}_{xy}(k)$. In Figure 4, the predicted current response in the $\alpha\beta$ subspace has been represented using purple font. These vectors describe the direction in which the stator currents would evolve if the corresponding voltage vector were applied. The alignment between each candidate's current response direction and the reference current vector is quantified using the scalar product, as expressed in

$$J_n = \frac{\Delta i_{\alpha\beta} \cdot \hat{\imath}^{n}_{\alpha\beta}(k+1) + K_{xy} \cdot \Delta i_{xy} \cdot \hat{\imath}^{n}_{xy}(k+1)}{\left\|\Delta i_{\alpha\beta}\right\| \cdot \left\|\hat{\imath}^{n}_{\alpha\beta}(k+1)\right\| + K_{xy} \cdot \left\|\Delta i_{xy}\right\| \cdot \left\|\hat{\imath}^{n}_{xy}(k+1)\right\|}, \quad n = [1, 2, \ldots, N] \tag{14}$$

where N denotes the total number of control actions. The control action that maximizes the cosine of the angle between the reference current vector and the predicted current response direction J_n is selected as the optimal voltage vector to be applied during the next control period.

Once this control action has been selected, its corresponding application time needs to be determined. This second selection stage aims to minimize, for both subspaces, the mismatch between the reference current vector and the predicted current response produced by the selected voltage vector $\hat{\imath}^{S_{opt}}_{\alpha\beta xy}(k)$. The optimal control period can be computed from

$$T_s = \left(\Delta i_{\alpha\beta xy}\right)^T \cdot \frac{\hat{\imath}^{S_{opt}}_{\alpha\beta xy}(k+1)}{\left\|\hat{\imath}^{S_{opt}}_{\alpha\beta xy}(k+1)\right\|^2}. \tag{15}$$

The overall procedure has been illustrated in Figure 4. As can be observed, the algorithm first selects the control action whose predicted current response direction is best aligned with the required reference current vector. Then, by appropriately adjusting the control period within the admissible range $[T_{min}, T_{max}]$, the algorithm can extend or shorten the application time of the selected voltage vector in order to satisfy the reference trajectory more accurately. As a result, the current variation reaches the point indicated by the yellow marker in Figure 4, approaching very close to the reference.

3.2. Main Limitations

Despite the advantages offered by the considered approach [26], several limitations can be identified when it is applied within the framework of FCS-MPC for multiphase drives:

L1 A dual controller conflict appears: in direct control schemes, an important limitation arises from the use of a single voltage vector during each control period. In multiphase drives, there are multiple control objectives [29]: on the one hand, the currents in the main $\alpha\beta$ subspace must be regulated to achieve the desired torque and flux production, while, on the other hand, the currents in the secondary xy subspace should be minimized to reduce additional harmonic-related losses. Since a single switching state simultaneously affects all subspaces, it is not possible to independently regulate them [27]. Consequently, improving the current tracking in the main subspace commonly increases the undesired components in the secondary subspaces, and vice versa, degrading the overall current quality and control performance. This limitation becomes especially critical at medium and low switching

frequencies, where the reduced control capability aggravates the coupling between objectives. Furthermore, in variable sampling-time schemes, the control period itself becomes an additional degree of freedom, which can intensify the conflict between subspaces. For instance, the xy plane typically requires short control periods to limit harmonic current growth, whereas longer application times are usually preferable to improve torque and flux production in the main subspace.

L2 Priority is given to the direction over the magnitude: regardless of the required amplitude of the desired reference current vector, the current state-of-art methods [25,26,44–47] focus on the direction of this vector during the first optimization stage. Considering the existence of a minimum application time due to implementation restrictions, this approach may lead to a suboptimal response by overlooking the natural response as a viable option, while also increasing the switching frequency to compensate for past errors.

L3 Use of the complete set of switching vectors: this characteristic of the original version presented in [26] introduces two main limitations. The first is related to the appropriate selection of control actions, while the second concerns the associated computational burden. Focusing on the first limitation, among the active voltage vectors of the considered multiphase ED, the V_L set minimizes the generation of secondary components, as illustrated in Figure 2. Consequently, the use of alternative (non-large) active control actions may result in degraded performance in terms of secondary subspace component generation [22,30]. As a result, undesired current components are generated in these subspaces, leading to increased harmonic distortion in the phase currents and higher stator copper losses [48].

Concerning the second limitation, the use of the complete set of switching states increases the computational burden, since a larger number of candidate control actions must be evaluated at each control step. This aspect becomes particularly critical in predictive control implementations subject to strict real-time constraints [28,53]. In addition, transitions involving non-adjacent voltage vectors typically require multiple switching events, whereas transitions between adjacent large voltage vectors involve only a single commutation. Therefore, the inclusion of all switching states may increase the effective switching frequency without providing a proportional improvement in harmonic performance [42].

These limitations motivate the development of the control strategy proposed in this work, which aims to overcome the aforementioned drawbacks while preserving the advantages of the variable-sampling-time predictive control framework.

3.3. Proposed Method

This work proposes an adaptive-sampling-time model predictive control strategy based on multivector control actions, referred to as AST-MPC (Adaptive Sampling Time Model Predictive Control), which overcomes the limitations L1, L2, and L3 in order to provide a more competitive solution. The proposed AST-MPC maintains the structure of conventional variable-application-time schemes, with an outer speed control loop and an inner current control loop, as shown in Figure 5. In this proposed method, two main novelties are introduced to mitigate the aforementioned limitations. On the one hand, conventional single switching states are replaced by a reduced set of virtual voltage vectors [30], each one formed by a combination of three adjacent large vectors specifically designed to cancel, on average, the voltage contribution in the secondary xy subspace. In this manner, the regulation of the secondary components is inherently achieved in open-loop mode, mitigating the dual-controller conflict defined in L1 and allowing the predictive controller to focus exclusively on the current tracking task in the main $\alpha\beta$

subspace. Furthermore, the use of these multivector control actions significantly reduces the computational burden by decreasing the number of evaluated candidates and enabling the use of a reduced-order prediction model excluding secondary components, thus addressing L3. On the other hand, to mitigate the impact of L2, the proposed AST-MPC incorporates a threshold-based decision mechanism that accounts for the existence of minimum admissible application times and reduces the sequentiality in selecting the optimal control action.

Focusing on the designed AST-MPC structure (Figure 5), the external loop ensures the speed tracking using a proportional–integral (PI) controller. The reference i_q^* is the output of the outer control loop, while the reference i_d^* is set to a constant value to ensure proper machine magnetization. Using these references together with the estimated rotor position, the current references in the $\alpha\beta$ subspace $i_{\alpha\beta}^*(k+2)$ are obtained by applying the inverse Park transformation. The inner current control loop is composed of several sequential steps. First, the reference current vector $\Delta i_{\alpha\beta}$ is estimated (13), calculating the difference between the reference currents $i_{\alpha\beta}^*(k+2)$ and the measured currents expressed in the stationary reference frame after applying the Clarke transformation $i_{\alpha\beta}(k)$. Then, the predicted current response for each available control action is estimated using (12), along with the measured mechanical speed ω_m and the measured currents in the stationary frame $i_{\alpha\beta}(k)$. Taking into account the practical implementation constraints, the proposed method incorporates a one-step delay compensation approach, which is commonly employed in model predictive control schemes [54].

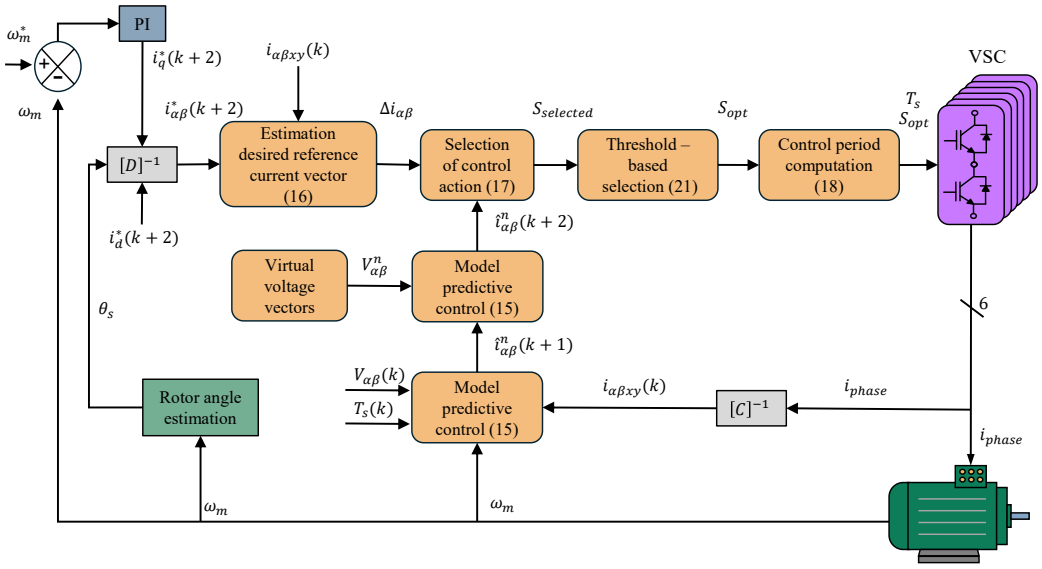


Figure 5. Schematic representation of the AST-MPC in a six-phase IM drive.

Regarding the employed active control actions to estimate the predicted current response in (12), they are formed into trios of adjacent large-voltage vectors [30]. They are designed offline, and their corresponding duty cycles are computed to satisfy two key conditions: the average voltage contribution in the secondary xy subspace is null, and the sum of the normalized application times must not exceed unity, ensuring a valid time allocation within the control period. In this manner, the proposed control strategy operates with a finite set of 13 admissible control actions, consisting of 12 virtual vectors and the null vector, thereby representing a significant reduction in the required evaluations. These control actions are specifically designed to, on average, cancel the voltage components in the secondary xy subspace. This feature enables an implicit open-loop regulation of this subspace, providing natural fault tolerance, reducing L1, and allowing the use of a reduced machine model that excludes the secondary components (L3).

Unlike conventional variable-sampling-time approaches, where the control action is selected exclusively according to its directional alignment with the desired reference current vector, the proposed AST-MPC introduces an additional validation stage aimed at evaluating the feasibility of the required current correction. In conventional VST-MPC schemes, once the control action providing the best alignment is selected, the variable sampling time is solely responsible for adjusting the magnitude of the response. However, due to the existence of minimum admissible application times imposed by practical implementation constraints, certain operating conditions may arise in which even the minimum achievable response of the selected active vector exceeds the required current correction. Under these conditions, the directional criterion alone becomes insufficient and may lead to overcorrection and unnecessary switching activity. To overcome this limitation, the proposed AST-MPC incorporates a threshold-based mechanism that evaluates whether the selected control action is capable of generating the desired current variation within the admissible operating range.

Then, the predicted current response of each available control action is evaluated using (14) to identify the control action that maximizes the scalar-product criterion and, consequently, to obtain the best alignment with the reference vector. After this directional selection stage, a threshold-based decision mechanism is introduced to mitigate L2. For the selected control action, two circular boundaries, D_{max} and D_{min}, are defined based on the magnitude of the predicted current response, applying maximum and minimum allowable application times:

$$\begin{aligned} D_{max} &= \left\| \hat{i}_{\alpha\beta}^{selected}(k+2) \right\| \cdot T_{max}, \\ D_{min} &= \left\| \hat{i}_{\alpha\beta}^{selected}(k+2) \right\| \cdot T_{min}. \end{aligned} \tag{16}$$

In addition, D, related to the magnitude of the reference vector, is estimated:

$$D = K_{Thr} \cdot \left\| \Delta i_{\alpha\beta} \right\|. \tag{17}$$

The following decision criterion is defined:

$$\begin{aligned} &\text{Case 1:} \quad D \geq D_{min} \Rightarrow S_{opt} = S_{selected}, \\ &\text{Case 2:} \quad D < D_{min} \Rightarrow S_{opt} = S_{null}. \end{aligned} \tag{18}$$

Therefore, the proposed threshold mechanism does not simply modify the selected control action, but introduces a supervisory decision layer over the conventional directional selection process. In this manner, the controller not only determines which voltage vector is better aligned with the reference, but also evaluates whether the corresponding current variation can be physically adjusted through the admissible sampling-time range.

If the Case 2 scenario appears, the selected active control action $S_{selected}$ is discarded, and the null action S_{null} is applied instead, since even the minimum actuation would exceed the required correction, and it is preferable to rely on the natural system dynamics. Otherwise, the selected control action is retained as optimal S_{opt}. This mechanism fundamentally modifies the conventional sequential decision process employed in previous VST-MPC approaches [25,26,44–47]. Instead of relying exclusively on directional alignment during the control action selection stage, the proposed AST-MPC additionally incorporates magnitude feasibility information through the threshold criterion. Consequently, the controller can distinguish between situations in which the active vector effectively reaches the reference and those in which the null vector provides a more suitable response, given the imposed minimum application time constraints. The impact of radius D can be adjusted through a weighting factor K_{Thr}, which allows tuning the trade-off between aggressive reference tracking and smoother control behavior with reduced switching activity. To facilitate the

understanding of the proposed criterion, Figure 6 provides a graphical illustration. As observed, D_{min} and D_{max} are constant, whereas D varies at each control period, depending on the desired reference current vector $\Delta i_{\alpha\beta}$ estimated. Finally, once the optimal control action S_{opt} has been determined, the corresponding application time, or equivalently the control period T_s, is calculated using (15), thus completing the control algorithm.

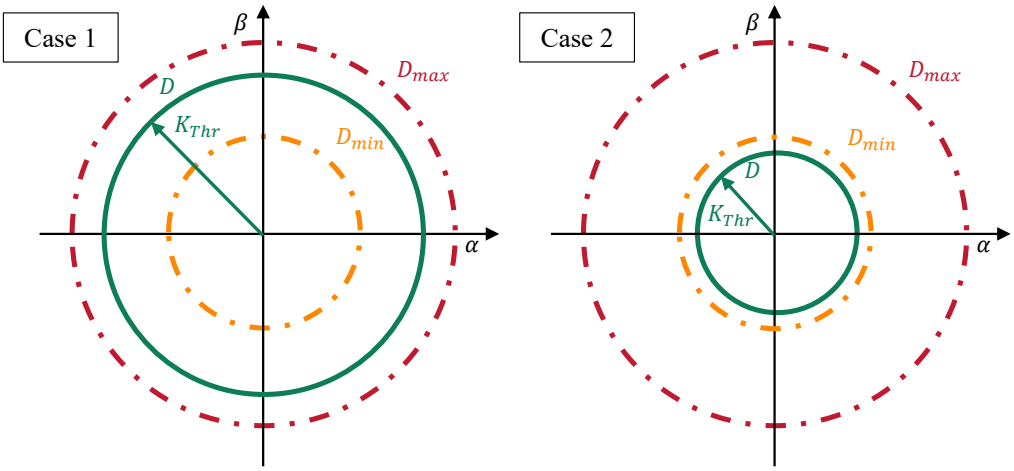


Figure 6. Graphical illustration of the threshold criterion used in the proposed control technique: Case 1 ($D \geq D_{min}$) and Case 2 ($D < D_{min}$).

To further clarify the sequence of operations and the interaction between the different stages of the proposed control strategy, Figure 7 presents a detailed flowchart of the AST-MPC algorithm. As shown, the control process starts with the estimation of the desired reference current vector and proceeds with the evaluation of all candidate control actions, where the predicted current response is obtained considering the one-step delay compensation [54]. Directional selection is then performed by maximizing the scalar product criterion, identifying the control action that provides the best alignment with the reference. Subsequently, the threshold-based mechanism evaluates the suitability of this action by comparing the required current variation with the minimum achievable effect. Depending on this condition, either the selected active vector is retained or replaced by the null vector. Finally, the corresponding application time is computed, completing the control cycle.

As a consequence of the implemented solution, the control objectives become effectively decoupled: the mitigation of secondary subspace components is inherently achieved by the definition of the control actions, while the predictive regulation strategy can focus exclusively on tracking the current references in the main subspace. This directly addresses one of the main drawbacks of conventional single-vector approaches, in which a single control action must simultaneously satisfy conflicting objectives, and enables improved current tracking performance without increasing control complexity. Additionally, the use of virtual vectors provides an inherent fault-tolerant capability [55]. In the event of an open-phase fault affecting one or more phases, the control strategy can continue operating without requiring any reconfiguration of the algorithm, thus enhancing the robustness of the overall drive system.

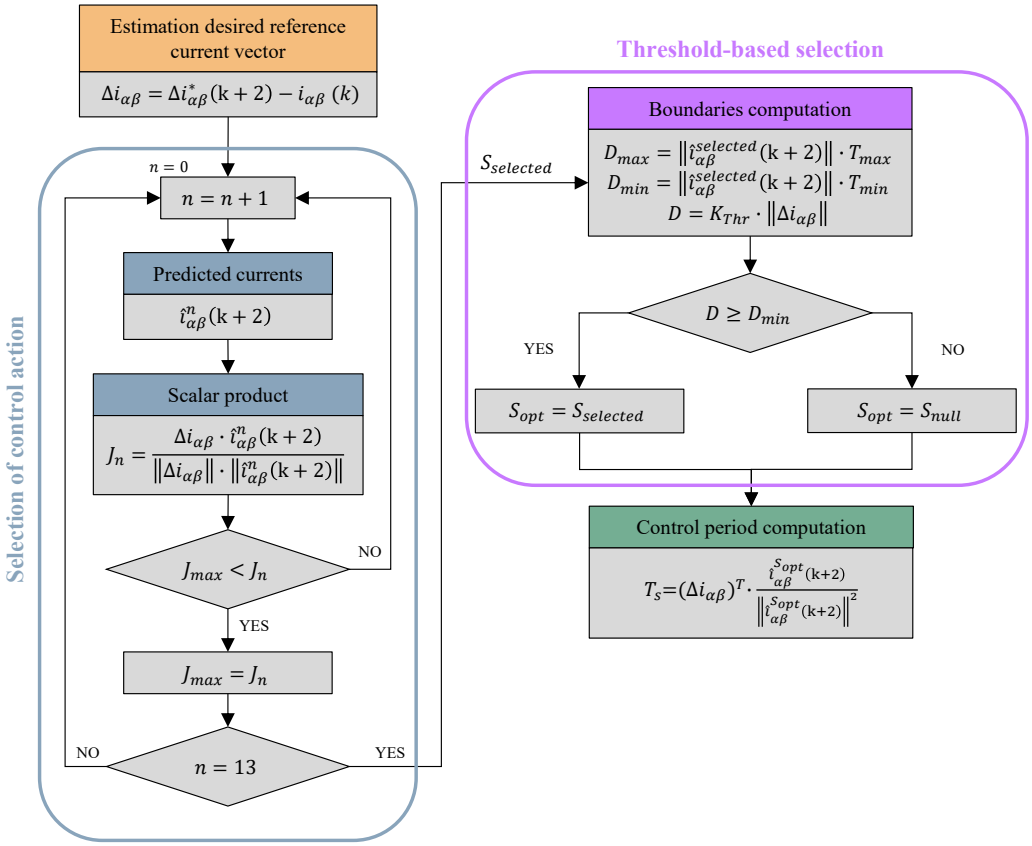


Figure 7. Flowchart of the proposed AST-MPC algorithm, including the selection of control action, threshold-based selection, and control period computation.

4. Experimental Validation

4.1. Test Bench Description

The experimental evaluation was carried out using the laboratory test bench shown in Figure 8, which served as the common platform for all control strategies considered in this work. The drive system consists of an asymmetrical six-phase induction machine with two three-phase stator windings spatially displaced by 30°. Each winding set is independently powered by a two-level three-phase voltage source VSC (VSC1 and VSC2), both implemented with Semikron SKS22F modules (Semikron Danfoss, Nuremberg, Germany). Although the VSCs share the same grid connection through a single transformer, their rectifier stages generate two electrically isolated DC-links with identical characteristics. The electrical parameters of the machine, summarized in Table 2, were obtained through a combination of AC time-domain tests [56] and standstill experiments with VSC excitation [57].

All real-time control algorithms have been implemented on a Texas Instruments TMS320F28335 digital signal processor (Texas Instruments, Dallas, TX, USA), programmed via JTAG using Code Composer Studio (v5.3). Stator phase currents were measured with Hall-effect sensors (LEM LAH 25-NP, LEM, Geneva, Switzerland), while rotor mechanical speed was captured using an incremental optical encoder (GHN510296R, Renishaw, Wotton-under-Edge, UK).

The six-phase induction machine shaft is directly coupled to a DC generator, whose armature circuit feeds a configurable resistive load. This configuration allows the generated electrical power to be dissipated and produces a load torque that depends on both the operating speed and the selected armature resistance. The armature resistance, which

determines the load level applied to the induction machine, has been configured for three different values corresponding to distinct load conditions, as summarized in Table 3.

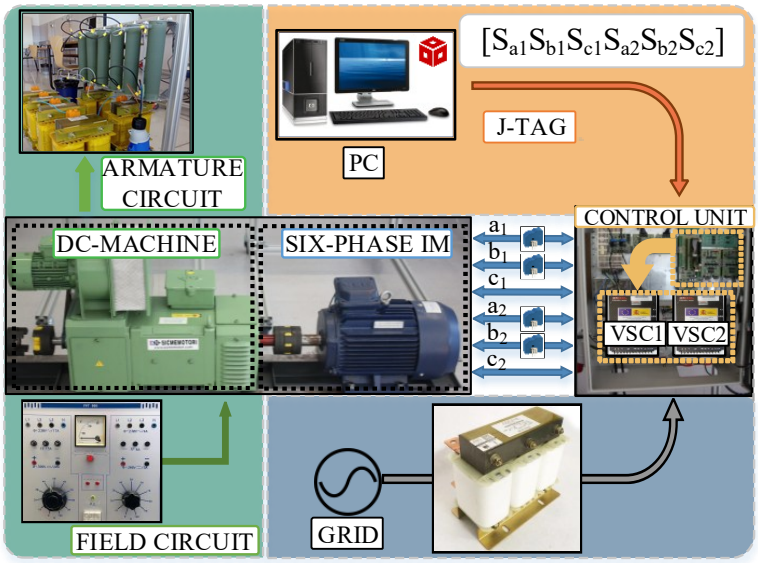


Figure 8. Diagram of the test rig employed to evaluate the control schemes.

Table 2. Six-phase IM test bench and control parameters.

Parameter	Description	Value
V_{dc} (V)	DC-link voltage	325
I_{peak} (A)	Peak current	4.5
R_s (Ω)	Stator resistance	4.19
R_r (Ω)	Rotor resistance	3.2
L_m (mH)	Mutual inductance	280
L_{ls} (mH)	Stator leakage inductance	4.2
L_{lr} (mH)	Rotor leakage inductance	55.1
p (-)	Number of pole pairs	3
ω_n (rpm)	Rated speed	1000
P_n (kW)	Rated power	1
τ_n (Nm)	Rated torque	10
T_{min} (μs)	Minimum sampling time	66.67
T_{max} (μs)	Maximum sampling time	100

Table 3. Load configurations connected to the DC generator.

Identification	Description	Resistance (Ω)
R1	Low torque operating configuration	100
R2	Medium torque operating configuration	50
R3	High torque operating configuration	33.33

4.2. Experimental Results

This section presents an experimental assessment of the proposed AST-MPC strategy, focusing on a detailed analysis of its behavior and performance under different operating conditions. The objective is to highlight the advantages of the proposed method by comparing it with two alternative FCS-MPC-based control schemes that represent different combinations of control actions and sampling time characteristics. In particular, the proposed AST-MPC is evaluated against a variable sampling time predictive control strategy that applies a single voltage vector per control period, referred to as LP-MPC [26], and

against a multi-vector predictive control scheme operating with a fixed sampling time, denoted as TV-MPC [30], which applies three large voltage vectors during each control period. This comparison enables a comprehensive evaluation of the impact of both sampling time adaptation and multi-vector control actions on the overall performance of the multiphase drive.

It should be noted that the LP-MPC strategy considered in this work corresponds to an enhanced version of the approach originally presented in [26]. In the formulation reported in [26], the predictive controller evaluates the complete set of switching states available in the motor drive. In contrast, the implementation adopted in this work restricts the candidate control actions to large voltage vectors and the null vector. This modification is introduced to improve the practical performance of the baseline method while preserving its original control philosophy, and is consistent with well-established practices in the literature [20,37]. The use of large voltage vectors provides several advantages, including reduced switching losses due to simpler transitions, improved dc-link voltage utilization in the main $\alpha\beta$ subspace, and lower harmonic distortion as a consequence of their reduced projection in the secondary xy subspace [58]. Additionally, limiting the candidate set contributes to reducing the computational burden [28].

It is important to emphasize that this modification does not compromise the fairness of the comparison. On the contrary, the resulting LP-MPC implementation represents a more optimized and practically oriented version of the original method, providing a more competitive benchmark solution. Furthermore, all evaluated VSTLP control strategies have been implemented under identical conditions, including the same sampling frequency range, controller parameters, delay compensation strategy, and computational resources. This ensures that the observed performance differences are exclusively due to the control strategy itself, thus enabling a fair and consistent comparison framework for the proposed AST-MPC approach.

To facilitate the discussion and provide a clearer interpretation of the experimental results, this section is organized into six complementary analyses. First, the effectiveness of the proposed threshold-based mechanism and the influence of the parameter K_{Thr} are experimentally validated. Then, a steady-state comparative analysis between the proposed AST-MPC strategy and the benchmark control methods is presented [26,30]. Subsequently, the adaptive behavior of the variable-sampling-time mechanism is analyzed using histograms of control frequency selection under different operating conditions. After that, the dynamic performance of the proposed strategy is evaluated under speed transient conditions. The fault-tolerant capability of the proposed AST-MPC approach is then experimentally assessed under open-phase fault operation. Finally, a computational burden analysis is conducted to evaluate the implementation complexity of the analyzed control strategies.

4.2.1. Assessment 1: Validation Threshold Mechanism

To validate the effectiveness of the proposed threshold-based mechanism, Figure 9 compares the behavior of the AST-MPC strategy when the threshold criterion is active and inactive. As observed in Figure 9a, the absence of the threshold mechanism leads to a noticeable degradation of the phase current quality despite the increase in switching activity. This behavior is associated with the exclusive use of the directional selection criterion, which may force the controller to apply active voltage vectors even when the required current correction cannot be applied. Under these conditions, the selected control actions can produce excessive current variations that must later be compensated by subsequent switching actions, resulting in increased oscillations and degraded current waveforms.

This effect can be more clearly appreciated in the control frequency selection histograms shown in Figure 9b. Without the threshold mechanism, the controller tends to operate much more frequently near the upper limit of the admissible frequency range, significantly increasing the effective switching frequency (f_{sw}). In contrast, when the threshold criterion is activated, the controller is capable of identifying situations where the null vector provides a more suitable response than the selected active vector, thus avoiding unnecessary switching actions. Quantitatively, the proposed threshold-based mechanism achieves a switching frequency reduction of 46.09% while simultaneously improving the current total harmonic distortion (THD) by 14.64% compared to the case without the threshold mechanism. These results experimentally confirm the relevance of incorporating magnitude-feasibility information into the decision-making process of the proposed AST-MPC strategy.

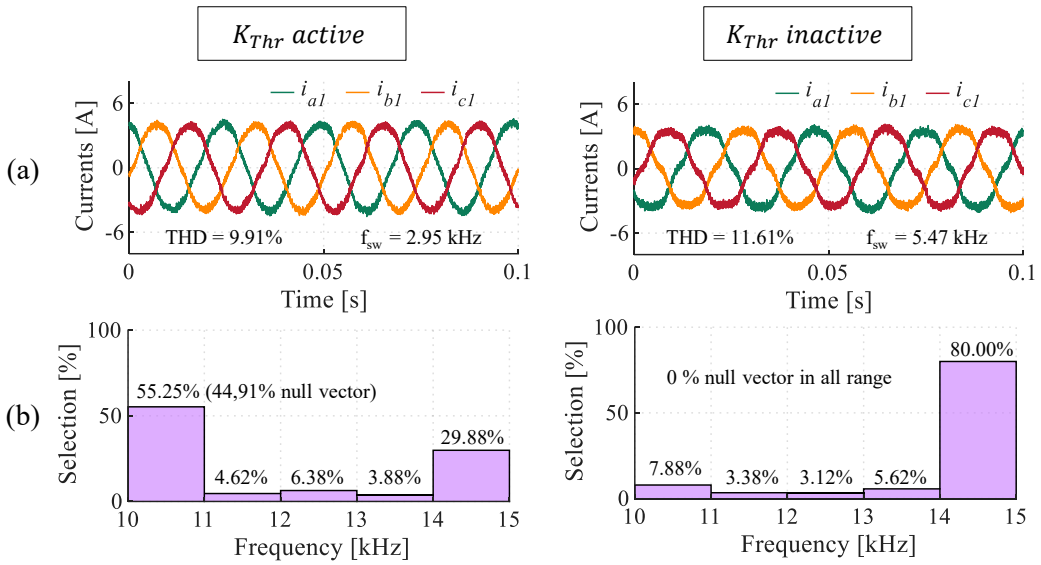


Figure 9. Experimental compariso n of the proposed control strategy with the threshold mechanism K_{Thr} active and inactive: (**a**) phase currents and (**b**) control frequency selection histograms.

Figure 10 presents the influence of the threshold parameter K_{Thr} on the performance of the proposed AST-MPC strategy, highlighting its direct impact on the trade-off between switching activity, current quality, and tracking performance. For $K_{Thr} = 1$, the control strategy promotes an extensive use of the null vector, as reflected in the frequency selection histograms. This results in a reduction in switching frequency and a slight improvement in current quality, with a relative THD reduction of 3.94% and a switching frequency decrease of 6.55% compared to the case $K_{Thr} = 1.5$. However, this benefit comes at the expense of degraded tracking performance in the dq subspace, as the current tracking error (ϵ_{dq}) increases from 0.0488 to 0.0684, representing a degradation of 28.65%. This behavior is associated with the limited voltage capability caused by the excessive selection of the null vector, which prevents the controller from properly driving the currents towards their references. In contrast, for $K_{Thr} = 2$, the influence of the threshold mechanism is significantly reduced, leading to a behavior closer to a purely directional selection strategy. Although this slightly improves the current tracking accuracy with respect to $K_{Thr} = 1.5$, it results in increased switching activity and a degradation in THD due to more frequent and, in some cases, less efficient switching actions. Therefore, this configuration prioritizes tracking performance at the expense of current quality. Based on this analysis, $K_{Thr} = 1.5$ is selected as a suitable compromise, as it provides the most balanced performance among all considered metrics. This value achieves reduced switching

frequency and improved current quality compared to higher threshold values, while maintaining a significantly better tracking accuracy than lower threshold values, without introducing a pronounced degradation in any performance indicator. For this reason, all experimental results presented throughout the manuscript for the proposed AST-MPC strategy have been obtained using $K_{Thr} = 1.5$.

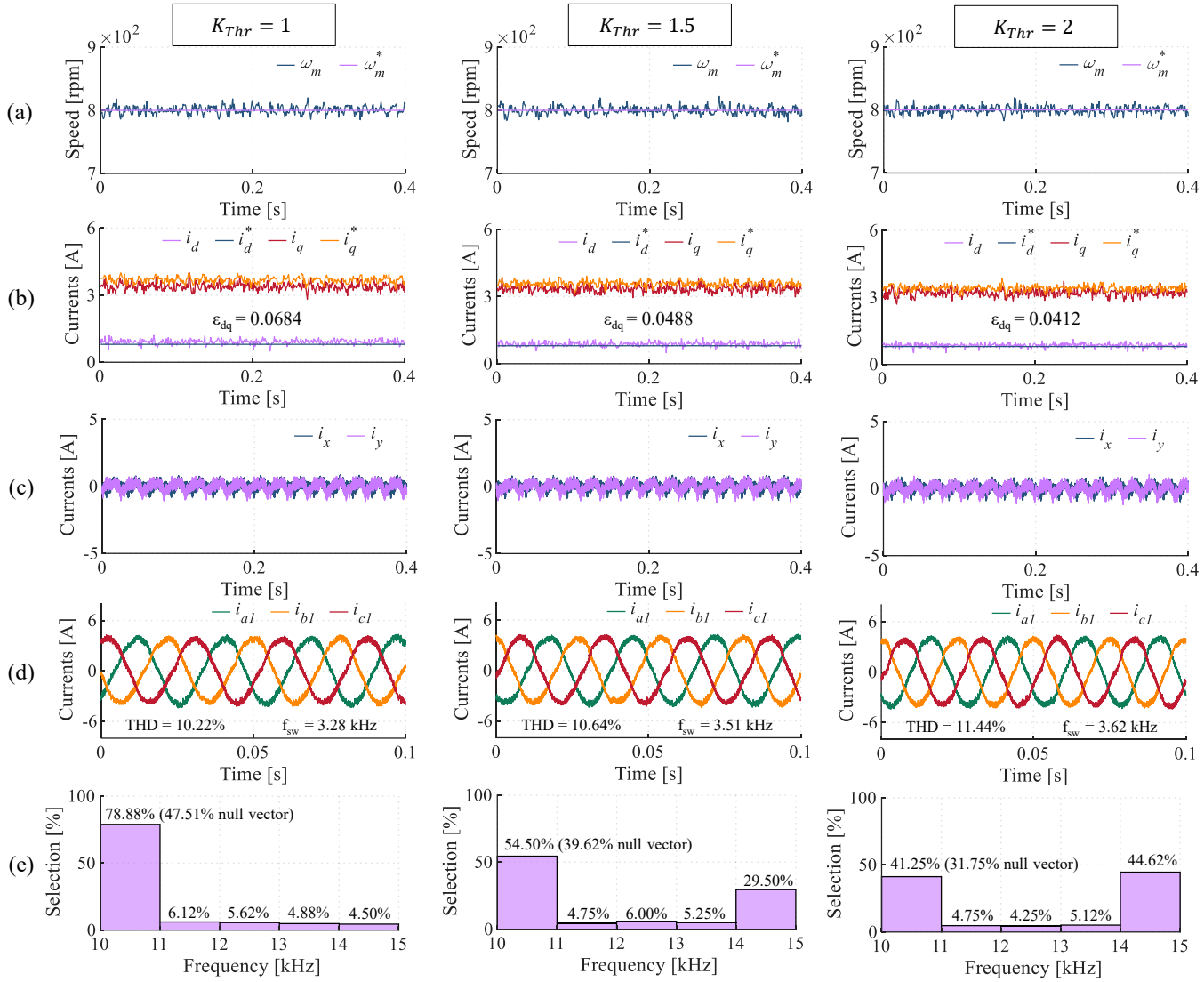


Figure 10. Influence of the threshold parameter K_{Thr} on the performance of the proposed AST-MPC strategy. (**First column**) $K_{Thr} = 1$, (**second column**) $K_{Thr} = 1.5$, and (**third column**) $K_{Thr} = 2$. From top to bottom: (**a**) speed response, (**b**) dq currents with tracking error, (**c**) xy currents, (**d**) phase currents with THD and switching frequency, and (**e**) control frequency selection histograms.

4.2.2. Assessment 2: Steady-State Analysis

Figure 11 presents the experimental results obtained with the three control strategies for an operating point of 500 rpm under load configuration R2. Figure 11 summarizes the main drive variables in order to facilitate a direct comparison between the evaluated control schemes: (a) rotor speed, (b) dq currents, (c) xy currents, (d) phase currents, and (e) histograms of control frequency selection. For the regulation strategies operating with variable sampling time, the admissible control frequency range was defined between 10 kHz and 15 kHz, whereas the fixed sampling time method operates at the maximum value of this range, 15 kHz. Under these conditions, the results allow analyzing the influence of both the control structure and the sampling strategy to be clearly assessed.

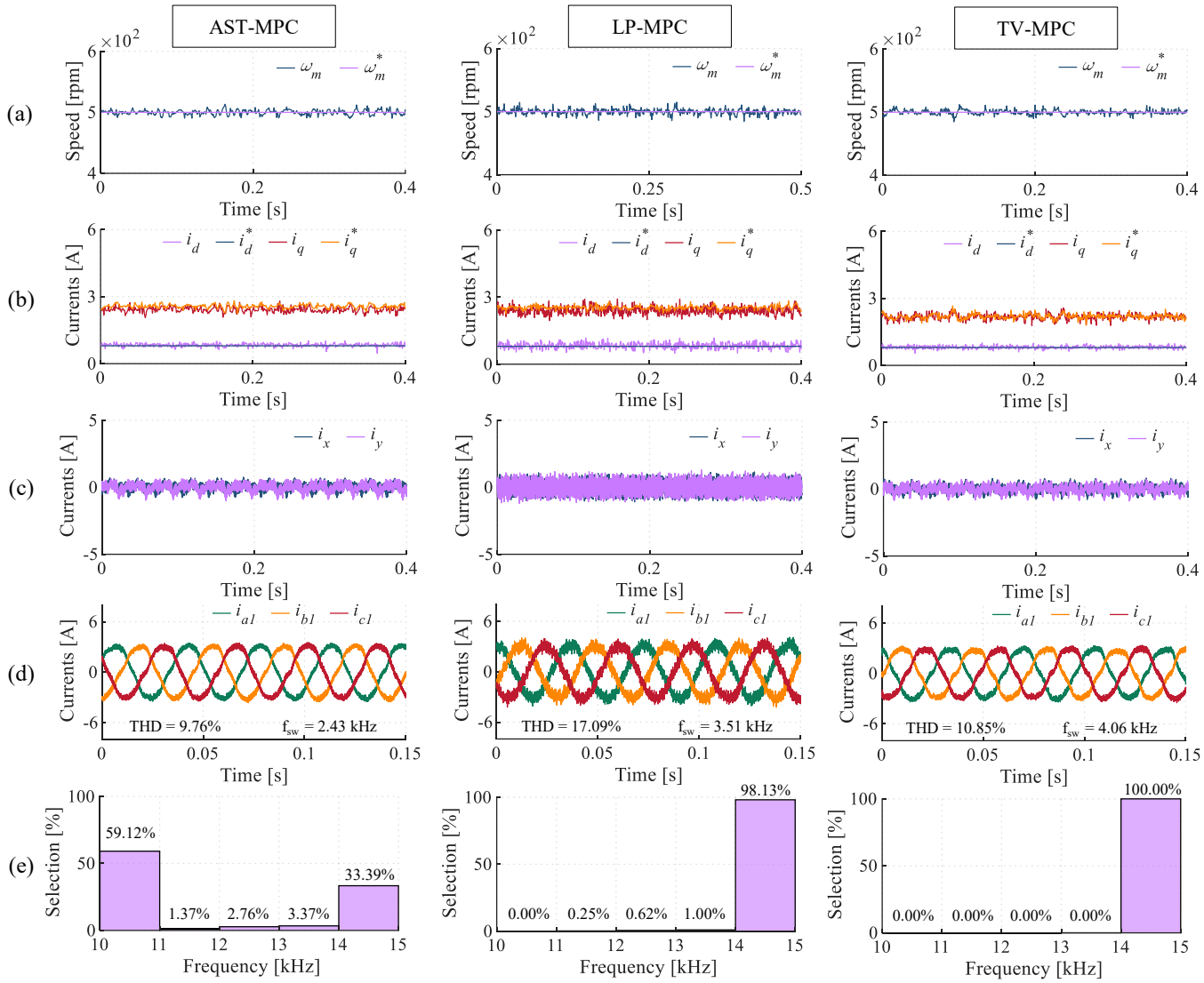


Figure 11. Experimental results obtained with AST-MPC (**first column**), LP-MPC (**second column**), and TV-MPC (**third column**). From top to bottom: (**a**) speed, (**b**) dq currents, (**c**) xy currents, (**d**) phase currents, and (**e**) control frequency selection histograms.

The speed responses shown in Figure 11a indicate that all the considered strategies provide an adequate tracking of the speed reference under the evaluated operating conditions, with no appreciable differences among them. However, more evident distinctions arise when analyzing stator current regulation. The dq current responses depicted in Figure 11b show that reference tracking is achieved in all cases, but the LP-MPC strategy exhibits clearly higher ripple levels in both the d- and q-axis components. This behavior is mainly associated with two factors: the use of a single voltage vector per control period and the consideration of both subspaces in the cost function. In contrast, the multivector control schemes (TV-MPC and AST-MPC) provide a significantly smoother current response, confirming the benefits of the regulation of secondary components in open-loop mode. A similar tendency can be observed in the xy subspace currents shown in Figure 11c, where both multivector strategies maintain the secondary subspace currents at significantly lower levels than those obtained with LP-MPC. This result reflects the difficulty of the single-vector approach to simultaneously achieve an accurate tracking of the dq current references while minimizing the undesired current components associated

with the secondary xy subspace, which are directly related to additional stator copper losses. The impact of these differences becomes more evident when examining the phase currents presented in Figure 11d, where the multivector control strategies produce a clear improvement in current waveform quality. In quantitative terms, the THD is reduced by 36.51% for TV-MPC relative to LP-MPC and by 42.89% for the proposed AST-MPC strategy, highlighting the advantages of multivector control actions for improving current quality in multiphase drives.

A particularly relevant advantage of the proposed method becomes apparent when considering the switching frequency. Despite achieving the best current quality among the evaluated controllers, the AST-MPC strategy requires significantly lower switching activity. Specifically, it achieves a current quality comparable to that of TV-MPC while reducing the switching frequency by 40.14%, and even 30.76% lower than LP-MPC, despite the latter applying only one voltage vector per control period. This behavior can be understood from the frequency selection histograms shown in Figure 11e. Although LP-MPC operates with variable sampling time, the controller is forced to select frequencies close to the upper limit of the admissible range in order to satisfy the control objectives using a single control action, resulting in 98.13% of the selections occurring near the maximum frequency. In contrast, the proposed AST-MPC strategy makes a more effective use of the entire available frequency range, allowing lower control frequencies whenever possible while maintaining proper current regulation. This improved utilization of the frequency range explains how AST-MPC can apply three voltage vectors per control interval while still achieving a lower effective switching frequency than the other evaluated strategies.

Figure 12 provides a broader comparison of the main quality metrics across the operating range of the drive. In Figure 12, each row presents a 3D surface representation of the function of speed and load configuration, together with its corresponding projections for each variable independently. The evaluated performance indicators are as follows: (a) THD, (b) standard deviation of the xy currents (σ_{xy}), (c) f_{sw}, and (d) torque ripple (σ_{τ}). This analysis over multiple operating conditions allows a more global evaluation of the regulation schemes, demonstrating that the favorable performance observed in the operating point previously discussed in Figure 11 is not limited to that specific case but is consistently maintained across the explored speed and load range.

Focusing on Figure 12a, which depicts THD, a clear trend can be identified. From the distribution of the points and their projections, the LP-MPC strategy exhibits a noticeably higher dispersion of THD values, regardless of whether the variation is analyzed with respect to speed or load independently. Moreover, its THD levels remain consistently higher than those obtained with the multivector control schemes. In contrast, the multivector strategies present a much more compact distribution of THD values, indicating a more consistent current quality across the operating range. Within these approaches, the proposed AST-MPC method generally achieves slightly lower THD values than TV-MPC. The behavior of σ_{xy}, shown in Figure 12b, also reveals a clear global tendency. As both speed and load increase, the magnitude of the currents circulating in the secondary subspace tends to increase, resulting in higher standard deviation values. As expected, the largest values correspond to LP-MPC, since this method does not actively regulate the xy currents due to the inherent limitations of applying a single control action per control period. In contrast, the multivector control schemes significantly reduce the magnitude of these components, and the results obtained with AST-MPC and TV-MPC are almost indistinguishable, with both surfaces appearing practically superimposed. This confirms that both strategies provide an effective regulation of the secondary subspace currents. The f_{sw} results shown in Figure 12c reveal a different tendency. For the multivector control schemes, the f_{sw} generally increases as the operating point becomes more demanding,

i.e., when speed or load increases. This behavior is expected, as the control strategy must react more frequently to maintain the desired current-tracking performance. Among the evaluated methods, TV-MPC consistently exhibits the highest f_{sw} due to its use of a fixed, high control frequency and the application of three voltage vectors per control period. In contrast, the proposed AST-MPC strategy achieves the lowest switching frequency values in most operating conditions, benefiting from the adaptive sampling-time mechanism. The LP-MPC approach shows the opposite trend, as its switching frequency tends to decrease when the operating point becomes more demanding. As a result, the AST-MPC strategy generally outperforms both benchmark methods in this metric, with LP-MPC only reaching comparable or slightly lower switching frequency values at the most demanding operating points. Finally, Figure 12d presents the torque ripple, expressed through the standard deviation of the electromagnetic torque σ_τ. A general trend can again be observed: as the operating conditions become more demanding, the torque ripple increases. The highest torque ripple levels correspond to LP-MPC, which is consistent with its poorer dq current regulation capability. Conversely, the multivector control strategies exhibit significantly lower ripple levels, with AST-MPC and TV-MPC showing very similar behavior across the entire operating range and no noticeable differences between their surfaces.

Overall, the analysis across the different operating points confirms the main strengths of the proposed method. The AST-MPC strategy achieves high current quality, generally equal to or superior to the other evaluated control strategies, while maintaining effective regulation of both the dq and xy current components comparable to that of TV-MPC, but with a significantly lower switching effort. This combination of improved current quality and reduced switching activity highlights the advantages of integrating adaptive sampling time with multi-vector predictive control in multiphase drive applications.

4.2.3. Assessment 3: Adaptive Time Analysis

Figure 13 focuses exclusively on the behavior of the proposed AST-MPC strategy and illustrates the histograms of control frequency selection for three representative operating points, arranged from a low-demand condition to a high-demand one from the first to the third column. In addition to the frequency selection itself, Figure 13 also indicates, for each selected frequency, the percentage of control actions associated with null and active voltage vectors. This representation allows the adaptive behavior of the proposed regulation scheme to be clearly visualized, showing how the control algorithm modifies its decision-making process depending on the operating conditions of the drive.

For the low-demand operating point, most of the control actions are concentrated in the lowest portion of the available frequency range (left column, Figure 13), and all of them correspond to the selection of the null vector. Only a small portion of the control actions occurs at frequencies close to the upper limit of the admissible range, which are associated with the application of active voltage vectors required to maintain proper current regulation. Notably, intermediate frequencies are not selected in this operating condition, indicating that the controller naturally favors the lowest possible control frequency.

When the operating point moves to a medium-demand condition, the distribution of selected frequencies changes noticeably (see the middle column of Figure 13). The percentage of selections in the lowest frequency region decreases, while a larger portion of the control actions is distributed across intermediate and high frequencies, particularly near the upper limit of the admissible range. As shown in Figure 13, when the AST-MPC method operates at the lowest frequencies, the majority of the applied actions correspond to null vectors, representing 57.25% out of the total 59.12% of selections in this frequency region, while the remaining percentage corresponds to active voltage vectors. This behavior indicates that, although the scheme still exploits low frequencies when possible, the

increased control effort required at this operating point leads to a more diverse use of the available frequency range.

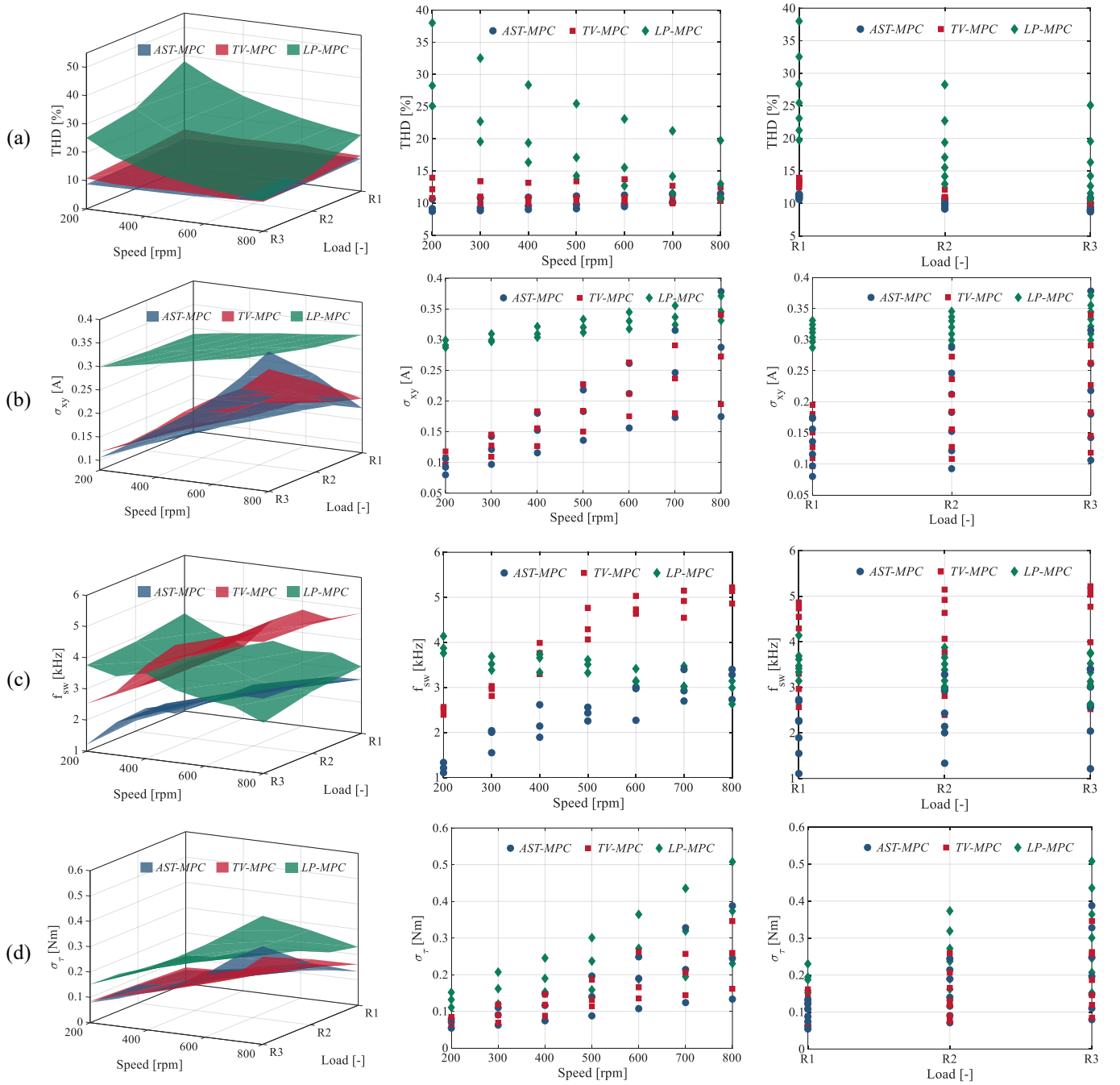


Figure 12. Operating metrics comparison of AST-MPC (blue), TV-MPC (red), and LP-MPC (green). For each row, a 3D surface (**first column**) and its projections onto XZ (**second column**) and YZ (**third column**) planes: (**a**) THD, (**b**) σ_{xy} , (**c**) f_{sw}, and (**d**) σ_τ.

At the highest-demand operating point, the percentage of selections in the lowest-frequency region is further reduced, and the control actions become more distributed across intermediate and high frequencies (see right, Figure 13). In particular, the use of intermediate frequencies increases considerably compared to the previously discussed cases. Additionally, the proportion of null and active vectors associated with the lowest frequencies becomes more balanced, with approximately 24.37% corresponding to null vectors and 26.63% to active vectors within the 51% of selections in this frequency region. This

indicates that, even at lower frequencies, the controller must apply active voltage vectors more frequently to meet the higher voltage requirements imposed by the operating point.

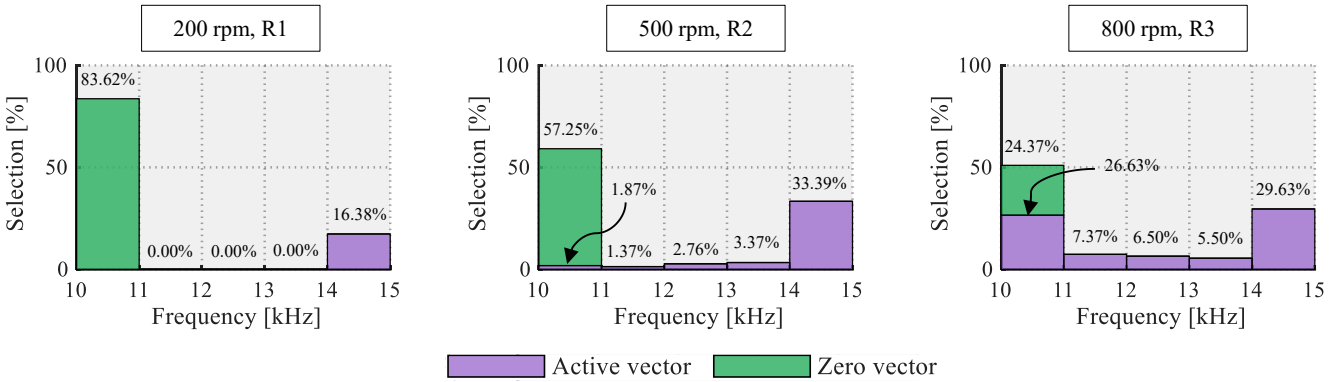


Figure 13. Frequency selection histograms for configuration at 200 rpm—R1 (**first column**), 500 rpm—R2 (**second column**), and 800 rpm—R3 (**third column**).

All in all, the results presented in Figure 13 clearly illustrate the adaptive capability of the proposed AST-MPC strategy, which intelligently adjusts the control frequency according to the instantaneous operating requirements of the drive. An important observation is that whenever the optimal control action corresponds to the null vector, the controller consistently selects frequencies within the lowest region of the admissible range, thus minimizing unnecessary switching activity while preserving adequate control performance.

4.2.4. Assessment 4: Dynamic Analysis

Figure 14 presents the dynamic response of the proposed AST-MPC strategy to a step change in the speed reference from 400 rpm to 800 rpm. Figure 14 illustrates the evolution of the main drive variables during the transient: (a) rotor speed, (b) dq currents, (c) xy currents, and (d) phase currents. This test is intended to evaluate the capability of the proposed control scheme to properly regulate the drive under transient conditions and to verify that the favorable steady-state performance discussed previously is not achieved at the expense of degraded dynamic behavior. As shown in Figure 14a, when the speed reference is modified, the designed AST-MPC achieves a suitable response to satisfy the reference value. A similar behavior can be observed in the dq current responses shown in Figure 14b, where the current components quickly adapt to the new operating conditions while maintaining an appropriate tracking of their respective references. These results confirm that the proposed control strategy also preserves a suitable dynamic response. The transient behavior can also be observed in the xy currents and phase currents shown in Figure 14c and Figure 14d, respectively. In these waveforms, the change in the operating point results in an almost instantaneous adjustment of the current amplitude, reflecting the rapid response of the AST-MPC scheme to the new speed reference. Despite the sudden variation in the operating conditions, the currents remain well regulated, and no significant oscillations appear during the transient. Overall, this test demonstrates that the proposed control strategy not only provides the favorable steady-state performance discussed in the previous figures but also maintains a fast and well-damped dynamic response, confirming the robustness of the method under varying operating conditions.

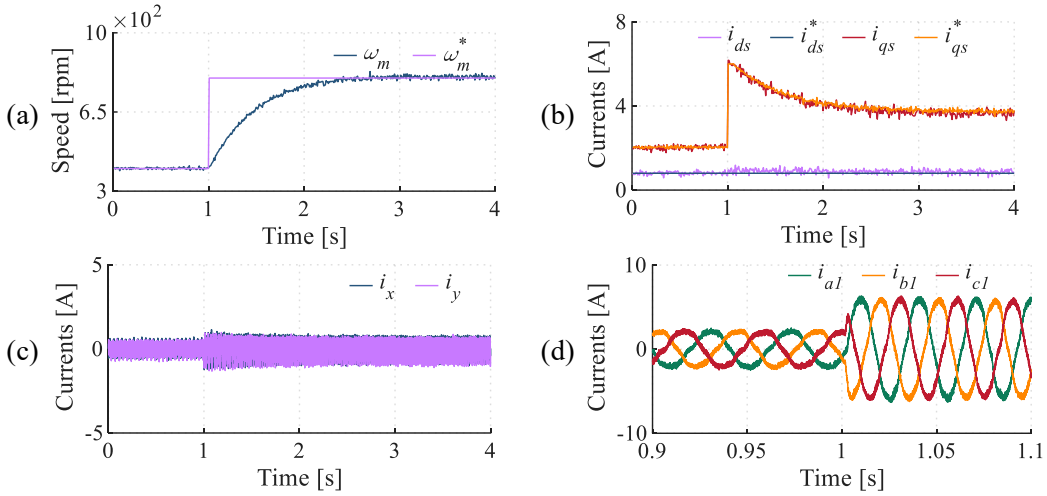


Figure 14. Dynamic response of the proposed method to a speed reference step from 400 rpm to 800 rpm: (**a**) speed, (**b**) dq currents, (**c**) xy currents, and (**d**) phase currents.

To complement the qualitative analysis derived from Figure 14, a quantitative evaluation of the transient performance has been carried out. The corresponding results are summarized in Table 4, where standard dynamic performance indices such as speed overshoot, settling time, recovery time, current peak, as well as speed and torque ripple are reported for the evaluated speed step condition. These metrics provide a more objective assessment of the system response and confirm the observations obtained from the experimental waveforms. In particular, the proposed AST-MPC strategy exhibits a well-balanced transient behavior, characterized by limited overshoot, appropriate settling dynamics, and controlled current peaks, while maintaining reduced oscillations in speed during the transient. This quantitative analysis reinforces the conclusion that the proposed method achieves a suitable steady-state without compromising the dynamic performance.

Table 4. Quantitative dynamic performance indices of the proposed control strategy under speed step condition (step from 400 rpm to 800 rpm).

Dynamic Metric	Value
Speed overshoot (%)	5.45
Speed settling time with 5% tolerance (s)	1.33
Speed recovery time (s)	0.78
q current peak (A)	6.07
Speed ripple (rpm)	15.72
Torque ripple (Nm)	0.31

4.2.5. Assessment 5: Fault-Tolerance Analysis

Figure 15 illustrates the post-fault behavior of the proposed control strategy when phase a_1 is opened during the experimental test. As observed in Figure 15a, the speed-tracking performance remains unaffected by the fault, maintaining accurate reference-following. Likewise, the dq current components shown in Figure 15b continue to track their references without noticeable degradation, confirming that the main control objective in the $\alpha\beta$ subspace is preserved. In contrast, the effect of the fault becomes evident in the secondary subspace, as shown in Figure 15c. This behavior is also reflected in the phase currents of Figure 15d, where phase a current drops to zero immediately after the fault, while the remaining phases continue operating in a stable manner. Finally, Figure 15e illustrates that the x component naturally evolves with an opposite trend to that of the α component, reflecting the inherent coupling imposed by the fault condition. In

summary, these results demonstrate that the proposed AST-MPC strategy exhibits natural fault-tolerant capability, maintaining satisfactory performance under open-phase fault conditions without requiring any control reconfiguration.

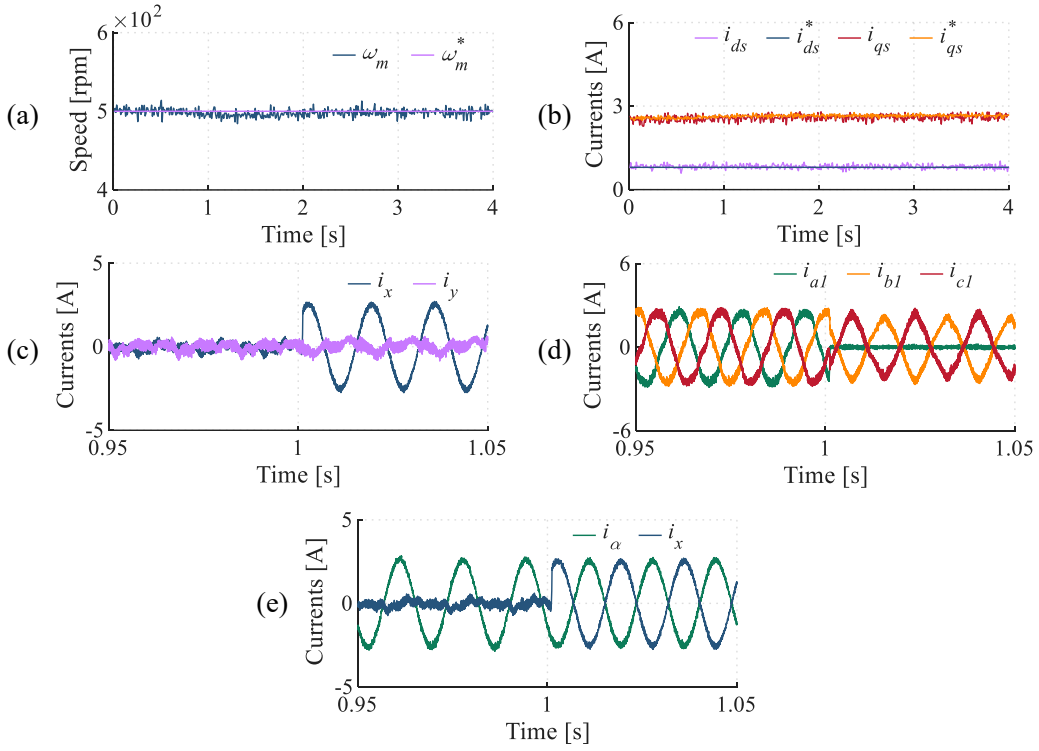


Figure 15. Post-fault response of the proposed method to a speed reference of 500 rpm: (**a**) speed, (**b**) dq currents, (**c**) xy currents, (**d**) phase currents, and (**e**) αx currents.

4.2.6. Assessment 6: Computational Burden Analysis

Table 5 summarizes the execution times associated with the different predictive control strategies considered in this work, including conventional FCS-MPC implementations considering the complete set of 64 switching states (FCS-MPC64) [15], reduced-vector implementations with 13 control actions (FCS-MPC13), LP-MPC implementations considering both 64 and 13 candidate control actions (LP-MPC64 and LP-MPC13) [26], the fixed-sampling-time multivector strategy (TV-MPC) [30], and the proposed AST-MPC approach. The reported results clearly highlight the computational advantage obtained by reducing the number of evaluated control actions through the use of predefined virtual voltage vectors.

Table 5. Execution time of different control schemes.

FCS-MPC64	FCS-MPC13	LP-MPC64	LP-MPC13	TV-MPC	AST-MPC
67.4 µs	22.0 µs	78.3 µs	31.2 µs	25.9 µs	27.1 µs

As observed, the conventional FCS-MPC64 scheme evaluating all 64 switching states requires an execution time of 67.4 µs, whereas the reduced-vector version FCS-MPC13, considering only 13 control actions, decreases the computational burden to 22.0 µs, representing a reduction of 67.36%. A similar tendency can be identified for the LP-MPC strategy, where execution time decreases from 78.3 µs in LP-MPC64 to 31.2 µs in LP-MPC13 when the candidate control set is reduced from 64 to 13 vectors. These results confirm that

limiting the evaluated control actions significantly improves the computational burden of predictive control schemes in multiphase drives.

Regarding the multivector strategies, TV-MPC and the proposed AST-MPC exhibit execution times of 25.9 µs and 27.1 µs, respectively. Although AST-MPC incorporates additional stages associated with the adaptive sampling time mechanism and the threshold-based decision criterion, the increase in execution time with respect to TV-MPC remains very limited. This demonstrates that the proposed AST-MPC strategy preserves a computational complexity comparable to that of conventional reduced-vector predictive control schemes while simultaneously providing the performance improvements discussed in the previous experimental analyses.

5. Conclusions

The proposed multivector AST-MPC has demonstrated superior performance compared to both fixed-sampling-time multivector schemes (TV-MPC) and variable-sampling-time single-vector approaches (LP-MPC). Experimental results confirm that AST-MPC achieves lower THD and reduced effective switching frequency in most operating conditions, while maintaining accurate current regulation. These improvements are achieved through the combined use of multivector control actions, a threshold-based mechanism to prioritize the current magnitude, and adaptive sampling time, enabling more efficient exploitation of the available control actions and switching frequency range.

Furthermore, the proposed method exhibits a suitable dynamic response, ensuring accurate reference tracking under transient conditions such as speed steps. Its adaptive nature enables effective adjustment across different operating points, as reflected in the automatic selection of control periods. In addition, AST-MPC, to the best of the authors' knowledge, constitutes the first variable-sampling-time predictive control scheme with inherent natural fault-tolerant capability. The proposed approach overcomes the main limitations of conventional schemes by incorporating multivector control actions to decouple control objectives and a threshold-based mechanism that introduces magnitude awareness into a direction-based selection process, resulting in a flexible and high-performance solution for multiphase electric drives.

Author Contributions: Conceptualization, R.L.-L. and I.G.-P.; methodology, R.L.-L. and I.G.-P.; software, R.L.-L. and P.M.-M.; validation, R.L.-L., P.M.-M., and J.C.-R.; formal analysis, R.L.-L., J.C.-R., J.J.A., and A.G.-P.; investigation, R.L.-L., P.M.-M., and J.C.-R.; resources, I.G.-P. and M.J.D.; data curation, R.L.-L., J.C.-R., J.J.A., and A.G.-P.; writing original draft preparation, R.L.-L., I.G.-P., J.C.-R., J.J.A., A.G.-P., P.M.-M., and M.J.D.; review and editing, R.L.-L., I.G.-P., J.C.-R., J.J.A., A.G.-P., P.M.-M., and M.J.D.; visualization, R.L.-L.; supervision, I.G.-P. and M.J.D.; project administration, I.G.-P. and M.J.D.; funding acquisition, I.G.-P. and M.J.D. All authors have read and agreed to the published version of the manuscript.

Funding: This work has been supported by the Spanish Government under the project PID2024-158852OB-I00.

Institutional Review Board Statement: Not applicable.

Informed Consent Statement: Not applicable.

Data Availability Statement: The original contributions presented in this study are included in the article. Further inquiries can be directed to the corresponding author.

Conflicts of Interest: The authors declare no conflicts of interest.

Abbreviations

The following abbreviations are used in this manuscript:

AST-MPC	Adaptive Sampling Time Model Predictive Control
FCS-MPC	Finite Control Set Model Predictive Control
TV-MPC	Triple-Vector Model Predictive Control
LP-MPC	Lead-Pursuit Model Predictive Control
ED	Electric Drive
IM	Induction Machine
6ph-IM	Six-Phase Induction Machine
VSC	Voltage Source Converter
dc-link	Direct Current Link
VSTLPC	Variable Sampling Time Lead Pursuit Control
VSD	Vector Space Decomposition
PI	Proportional-Integral
THD	Total Harmonic Distortion
ϵ_{dq}	Current Tracking Error in dq Subspace
f_{sw}	Switching Frequency
σ_{xy}	Standard Deviation of Secondary Subspace Currents
σ_{τ}	Torque Ripple
T_s	Sampling Time
T_{min}/T_{max}	Minimum/Maximum Sampling Time
S_{opt}	Optimal Control Action
$S_{selected}$	Selected Control Action
S_{null}	Null Control Action
D, D_{min}, D_{max}	Threshold-based Parameters
K_{Thr}	Threshold Weighting Factor

References

1. Frikha, M.A.; Croonen, J.; Deepak, K.; Benômar, Y.; El Baghdadi, M.; Hegazy, O. Multiphase Motors and Drive Systems for Electric Vehicle Powertrains: State of the Art Analysis and Future Trends. *Energies* **2023**, *16*, 768. [CrossRef]
2. Mercedes AMG EQS 53. Available online: https://mercedes-benz-media.co.uk/releases/1618 (accessed on 15 April 2026).
3. Onsal, M.; Demir, Y.; Aydin, M. A New Nine-Phase Permanent Magnet Synchronous Motor with Consequent Pole Rotor for High-Power Traction App. *IEEE Trans. Magn.* **2017**, *53*, 8700606. [CrossRef]
4. Rubino, S.; Bojoi, I.R.; Mandrile, F.; Armando, E. Modular Stator Flux and Torque Control of Multi-Three-Phase Induction Motor Drives. *IEEE Trans. Ind. Appl.* **2020**, *56*, 6507–6525. [CrossRef]
5. Robles, E.; Fernandez, M.; Andreu, J.; Ibarra, E.; Zaragoza, J.; Ugalde, U. Common-mode voltage mitigation in multiphase electric motor drive systems. *Renew. Sustain. Energy Rev.* **2022**, *157*, 111971. [CrossRef]
6. Levi, E.; Bojoi, R.; Profumo, F.; Toliyat, H.; Williamson, S. Multiphase induction motor drives—A technology status review. *IET Electr. Power Appl.* **2007**, *1*, 489–516. [CrossRef]
7. Yang, G.; Hussain, H.; Li, S.; Zhang, X.; Yang, J.; Lee, C.H.T. Design and Analysis of Universal Natural Fault-Tolerant SVPWM Strategy with Simplified Fault Diagnosis for Multiphase Motor Drives. *IEEE J. Emerg. Sel. Top. Power Electron.* **2023**, *11*, 4340–4354. [CrossRef]
8. BMW iX M60. Available online: https://www.motortrend.com/news/2023-bmw-ix-m60-xdrive50-edrive-electric-motors-explained (accessed on 15 April 2026).
9. Zhang, M.; Yuan, M.; Jiang, J. A Comprehensive Review of the Multiphase Motor Drive Topologies for High-Power Electric Vehicle: Current Status, Research Challenges, and Future Trends. *IEEE Trans. Transp. Electrif.* **2025**, *11*, 3631–3654. [CrossRef]
10. Peng, X.; Liu, Z.; Jiang, D. A review of multiphase energy conversion in wind power generation. *Renew. Sustain. Energy Rev.* **2021**, *147*, 111172. [CrossRef]
11. Levi, E. Advances in Converter Control and Innovative Exploitation of Additional Degrees of Freedom for Multiphase Machines. *IEEE Trans. Ind. Electron.* **2016**, *63*, 433–448. [CrossRef]
12. Liu, Z.; Li, Y.; Zheng, Z. A review of drive techniques for multiphase machines. *CES Trans. Electr. Mach. Syst.* **2018**, *2*, 243–251. [CrossRef]

13. Rahman, K.; Rahman, S.; Bhaskar, M.S.; Iqbal, A.; Khandakar, A.; Tariq, M.; Alamri, B. Field-Oriented Control of Five-Phase Induction Motor Fed From Space Vector Modulated Matrix Converter. *IEEE Access* **2022**, *10*, 17996–18007. [CrossRef]
14. Sultan, A.H.; Al-Badrani, H. Field Oriented Control for Seven Phase Induction Machine with Comparative Control Method. In Proceedings of the 2024 12th International Conference on Smart Grid (icSmartGrid), Setúbal, Portugal, 27–29 May 2024; pp. 844–849. [CrossRef]
15. Ayala, M.; Doval-Gandoy, J.; Rodas, J.; Gonzalez, O.; Gregor, R. Current control designed with model based predictive control for six-phase motor drives. *ISA Trans.* **2020**, *98*, 496–504. [CrossRef]
16. Cui, J.; Tao, T.; Zhao, W. Optimized Control Set Model Predictive Control for Dual Three-Phase PMSM with Minimum Error Duty Cycle Regulation. *IEEE Trans. Power Electron.* **2024**, *39*, 1319–1332. [CrossRef]
17. Abdel-Moneim, M.G.; Abdel-Azim, W.E.; Abdel-Khalik, A.S.; Hamad, M.S.; Ahmed, S. Model Predictive Current Control of Nine-Switch Inverter-Fed Six-Phase Induction Motor Drives Under Healthy and Fault Scenarios. *IEEE Trans. Transp. Electrif.* **2024**, *10*, 10125–10135. [CrossRef]
18. Serra, J.; Cardoso, A.J.M. A Simplified Model Predictive Control for Asymmetrical Six-Phase Induction Motors That Eliminates the Weighting Factor. *Machines* **2022**, *10*, 1189. [CrossRef]
19. Saeed, M.S.R.; Song, W.; Huang, L.; Yu, B. Double-Vector-Based Finite Control Set Model Predictive Control for Five-Phase PMSMs with High Tracking Accuracy and DC-Link Voltage Utilization. *IEEE Trans. Power Electron.* **2022**, *37*, 15234–15244. [CrossRef]
20. Wang, H.; Wu, X.; Zheng, X.; Yuan, X. Model Predictive Current Control of Nine-Phase Open-End Winding PMSMs with an Online Virtual Vector Synthesis Strategy. *IEEE Trans. Ind. Electron.* **2023**, *70*, 2199–2208. [CrossRef]
21. Rodriguez, J.; Garcia, C.; Mora, A.; Davari, S.A.; Rodas, J.; Valencia, D.F.; Elmorshedy, M.; Wang, F.; Zuo, K.; Tarisciotti, L.; et al. Latest Advances of Model Predictive Control in Electrical Drives-Part II: Applications and Benchmarking with Classical Control Methods. *IEEE Trans. Power Electron.* **2022**, *37*, 5047–5061. [CrossRef]
22. Aciego, J.J.; Gonzalez-Prieto, I.; Duran, M.J.; Gonzalez-Prieto, A.; Carrillo-Rios, J. Guiding the Selection of Multi-Vector Model Predictive Control Techniques for Multiphase Drives. *Machines* **2024**, *12*, 115. [CrossRef]
23. Xue, Z.; Niu, S.; Chau, A.M.H.; Luo, Y.; Lin, H.; Li, X. Recent Advances in Multi-Phase Electric Drives Model Predictive Control in Renewable Energy Application: A State-of-the-Art Review. *World Electr. Veh. J.* **2023**, *14*, 44. [CrossRef]
24. Zhao, Y.; Lipo, T. Space vector PWM control of dual three phase induction machine using vector space decomposition. In Proceedings of the 1994 IEEE Industry Applications Society Annual Meeting, Denver, CO, USA, 2–6 October 1994; Volume 1, pp. 742–749. [CrossRef]
25. Martin, C.; Barrero, F.; Arahal, M.R.; Duran, M.J. Model-Based Predictive Current Controllers in Multiphase Drives Dealing with Natural Reduction of Harmonic Distortion. *Energies* **2019**, *12*, 1679. [CrossRef]
26. Arahal, M.R.; Martín, C.; Barrero, F.; Durán, M.J. Assessing Variable Sampling Time Controllers for Five-Phase Induction Motor Drives. *IEEE Trans. Ind. Electron.* **2020**, *67*, 2523–2531. [CrossRef]
27. Gonçalves, P.; Cruz, S.; Mendes, A. Finite Control Set Model Predictive Control of Six-Phase Asymmetrical Machines—An Overview. *Energies* **2019**, *12*, 4693. [CrossRef]
28. Marsal, E.; Arahal, M.R.; Satué, M.G.; Perales, M. Review of Fast Computation Methods for Finite-State Predictive Control of Multi-Phase Drives. *Appl. Sci.* **2024**, *14*, 11774. [CrossRef]
29. Levi, E. Multiphase Electric Machines for Variable-Speed Applications. *IEEE Trans. Ind. Electron.* **2008**, *55*, 1893–1909. [CrossRef]
30. González-Prieto, A.; González-Prieto, I.; Duran, M.J.; Aciego, J.J.; Salas-Biedma, P. Current Harmonic Mitigation Using a Multi-Vector Solution for MPC in Six-Phase Electric Drives. *IEEE Access* **2021**, *9*, 117761–117771. [CrossRef]
31. da Paz, G.F.; Melo, V.F.M.B.; de Freitas, I.S.; de Sousa, R.P.R.; Salvadori, F. Virtual Vector Direct Torque Control for a Nine-Phase Induction Machine Drive System with Eight Active Voltage Vectors Emulating Virtual Voltage Vectors. *IEEE Trans. Power Electron.* **2024**, *39*, 9457–9469. [CrossRef]
32. Yan, L.; Zhang, X.; Yang, J.; Yang, G.; Deng, R. Synthetic Vectors-Based Predictive Control of Dual Three-Phase PMSMs for Current Harmonics Mitigation Considering Average Deception Effect. *IEEE J. Emerg. Sel. Top. Power Electron.* **2024**, *12*, 3103–3114. [CrossRef]
33. Luan, T.; Wang, Z.; Long, Y.; Zhang, Z.; Li, Q.; Zhu, Z.; Liu, C. Multi-Virtual-Vector Model Predictive Current Control for Dual Three-Phase PMSM. *Energies* **2021**, *14*, 7292. [CrossRef]
34. Luo, Y.; Niu, S. Predictive Current Control for Six-Phase PMSM Motor With Multi-Step Synthesis Based Virtual Vectors. *IEEE Trans. Energy Convers.* **2023**, *38*, 134–146. [CrossRef]
35. Shawier, A.; Abdel-Azim, W.E.; Abdel-Moneim, M.G.; Gadoue, S.; Samy Abdel-Khalik, A.; Ahmed, S. Optimized Virtual Vector Technique with Loss Minimization of Six Phase IM Under Low-Speed Operation for Electric Vehicles. *IEEE Trans. Transp. Electrif.* **2025**, *11*, 5748–5758. [CrossRef]
36. Yu, B.; Song, W.; Li, J.; Li, B.; Saeed, M.S.R. Improved Finite Control Set Model Predictive Current Control for Five-Phase VSIs. *IEEE Trans. Power Electron.* **2021**, *36*, 7038–7048. [CrossRef]

37. Serra, J.; Bento, F.; Ma, A.J.M. Zero-Sequence Current Mitigation Using a Virtual Voltage Vector Solution for MPC in Symmetrical Six-Phase Electric Drives with Single-Star and Hexagon Winding Configurations. *IEEE J. Emerg. Sel. Top. Power Electron.* **2025**, *13*, 1601–1614. [CrossRef]
38. Yu, B.; Song, W.; Guo, Y.; Saeed, M.S.R. A Finite Control Set Model Predictive Control for Five-Phase PMSMs with Improved DC-Link Utilization. *IEEE Trans. Power Electron.* **2022**, *37*, 3297–3307. [CrossRef]
39. Liu, Y.; Wu, X.; Wang, H. A Natural Fault-Tolerant Method for Six-Phase PMSM Using Model Predictive Current Control. In Proceedings of the 2025 IEEE International Conference on Predictive Control of Electrical Drives and Power Electronics (PRECEDE), Nanjing, China, 5–8 June 2025; pp. 1–6. [CrossRef]
40. Wang, H.; Zheng, X.; Yuan, X.; Wu, X. Enhanced Natural Fault-Tolerant Model Predictive Current Control in Nine-Phase Motor Drives Under Open-Phase Faults. *IEEE Trans. Energy Convers.* **2022**, *37*, 2449–2460. [CrossRef]
41. Chen, C.; Zhou, H.; Ye, C.; Tao, T. Natural Fault-Tolerant Model-Free Predictive Flux Control in Five-Phase PMSM Drives Under Any-Phase Open-Circuit Fault. *IEEE Access* **2025**, *13*, 31889–31898. [CrossRef]
42. Carrillo-Rios, J.; Aciego, J.J.; Gonzalez-Prieto, A.; Gonzalez-Prieto, I.; Duran, M.J.; Lara-Lopez, R. Remaining Secondary Voltage Mitigation in Multivector Model Predictive Control Schemes for Multiphase Electric Drives. *Machines* **2025**, *13*, 862. [CrossRef]
43. Huang, Q.; Kang, M. Model Predictive Current Control of Multiphase Motor at Low Carrier Ratio. *Electronics* **2021**, *10*, 591. [CrossRef]
44. Hoffmann, N.; Andresen, M.; Fuchs, F.W.; Asiminoaei, L.; Thøgersen, P.B. Variable sampling time finite control-set model predictive current control for voltage source inverters. In Proceedings of the 2012 IEEE Energy Conversion Congress and Exposition (ECCE), Raleigh, NC, USA, 15–20 September 2012; pp. 2215–2222. [CrossRef]
45. Arahal, M.R.; Martin, C.; Barrero, F.; Gonzalez-Prieto, I.; Duran, M.J. Model-Based Control for Power Converters with Variable Sampling Time: A Case Example Using Five-Phase Induction Motor Drives. *IEEE Trans. Ind. Electron.* **2019**, *66*, 5800–5809. [CrossRef]
46. Arahal, M.; Satué, M.; Barrero, F.; Colodro, F. Variable sampling period multi-phase predictive controller based on regions. *Control Eng. Pract.* **2024**, *151*, 106021. [CrossRef]
47. Barrero, F.; Bermúdez, M.; Arahal, M.R.; González-Prieto, I. Predictive Current Control of a Five-Phase Drive Using a Lead-Pursuit Strategy and Virtual Voltage Vectors. *Appl. Sci.* **2025**, *15*, 5604. [CrossRef]
48. Xu, J.; Odavić, M.; Zhu, Z.; Wu, Z.; Freire, N. Switching-Table-Based Direct Torque Control of Dual Three-Phase PMSMs with Closed-Loop Current Harmonics Compensation. *IEEE Trans. Power Electron.* **2021**, *36*, 10645–10659. [CrossRef]
49. Carrillo-Rios, J.; Gonzalez-Prieto, I.; Gonzalez-Prieto, A.; Duran, M.J.; Aciego, J.J. Long-Prediction Horizon FCS-MPC for Multiphase Electric Drives with a Selective Control Action Promotion. *IEEE Trans. Ind. Electron.* **2024**, *71*, 9982–9993. [CrossRef]
50. Arahal, M.R.; Satué, M.G.; Barrero, F.; Martínez-Heredia, J. Model Reference Adaptive Predictive Current Control of Six-Phase Induction Machine. *IEEE Trans. Ind. Electron.* **2025**, *72*, 10927–10934. [CrossRef]
51. Bayhan, N.; Koçak, Y. A Comparative Study of Discretization Methods for Model Predictive Current Control of Permanent Magnet Synchronous Motors. *Processes* **2026**, *14*, 14. [CrossRef]
52. Biswas, B.N.; Chatterjee, S.; Mukherjee, S.; Pal, S. A Discussion on the Euler Method: A Review. *Electron. J. Math. Anal. Appl.* **2013**, *1*, 294–317. [CrossRef]
53. Serra, J.; Jlassi, I.; Cardoso, A.J.M. A Computationally Efficient Model Predictive Control of Six-Phase Induction Machines Based on Deadbeat Control. *Machines* **2021**, *9*, 306. [CrossRef]
54. Hu, J.; Zhu, J.; Platt, G.; Dorrell, D.G. Model-predictive direct power control of AC/DC converters with one step delay compensation. In Proceedings of the IECON 2012—38th Annual Conference on IEEE Industrial Electronics Society, Montreal, QC, Canada, 25–28 October 2012; pp. 4892–4897. [CrossRef]
55. Salas-Biedma, P.; González-Prieto, I.; Durán, M.J.; Bermúdez, M.; Barrero, F. Multiphase current imbalance localisation method applied to natural fault-tolerant strategies. *IET Electr. Power Appl.* **2020**, *14*, 1421–1429. [CrossRef]
56. Yepes, A.G.; Riveros, J.A.; Doval-Gandoy, J.; Barrero, F.; Lopez, O.; Bogado, B.; Jones, M.; Levi, E. Parameter Identification of Multiphase Induction Machines with Distributed Windings—Part 1: Sinusoidal Excitation Methods. *IEEE Trans. Energy Convers.* **2012**, *27*, 1056–1066. [CrossRef]
57. Riveros, J.A.; Yepes, A.G.; Barrero, F.; Doval-Gandoy, J.; Bogado, B.; Lopez, O.; Jones, M.; Levi, E. Parameter Identification of Multiphase Induction Machines with Distributed Windings—Part 2: Time-Domain Techniques. *IEEE Trans. Energy Convers.* **2012**, *27*, 1067–1077. [CrossRef]
58. Geng, Q.; Qin, Z.; Jin, X.; Zhang, G.; Zhou, Z. Direct Torque Control of Dual Three-Phase Permanent Magnet Synchronous Motors Based on Master–Slave Virtual Vectors. *World Electr. Veh. J.* **2024**, *15*, 199. [CrossRef]

Disclaimer/Publisher's Note: The statements, opinions and data contained in all publications are solely those of the individual author(s) and contributor(s) and not of MDPI and/or the editor(s). MDPI and/or the editor(s) disclaim responsibility for any injury to people or property resulting from any ideas, methods, instructions or products referred to in the content.